A General Search for Supersymmetry in Compressed Scenarios Featuring a Novel Fake Lepton Estimation Method

Margaret Lazarovits

B.A. Physics, University of Chicago, 2018

Submitted to the graduate degree program in Department of Physics and Astronomy and the Graduate Faculty of the University of Kansas in partial fulfillment of the requirements for the degree of Master of Science.

Professor Chris Rogan, Chairperson

Committee members

Professor Alice Bean, Committee member

Professor Kyoungchul (KC) Kong, Committee member

Date defended: March 31, 2022

The Thesis Committee for Margaret Lazarovits certifies
that this is the approved version of the following thesis:

A General Search for Supersymmetry in Compressed Scenarios Featuring a Novel Fake Lepton Estimation Method

Professor Chris Rogan, Chairperson

Date approved: May 5, 2022

Abstract

The overarching, foundational theory of our universe, the Standard Model, is a powerful predictor of known physics. However, there are still open questions in this model of physics that are currently being explored, such as the nature of dark matter, the origin of matter/anti-matter asymmetry, and the potential unification of fundamental forces. One theory that could prove to be an answer to some of these questions is supersymmetry (SUSY), an extension of the Standard Model. This analysis searches for evidence of electroweak SUSY in compressed scenarios, where the mass of the parent sparticle is close to that of its invisible child. This paper describes an analysis with leptonic final states from proton-proton collisions at the Large Hadron Collider (LHC) with the Compact Muon Solenoid detector. In addition to analyzing events with the Recursive Jigsaw Reconstruction method, the analysis also presents a novel, shape-based method for estimating the fake leptonic background. Preliminary exclusion limits show sensitivity to higher parent sparticle masses and smaller, more compressed mass splittings than previously probed at the LHC.

Acknowledgements

Firstly, I would like to thank my advisor, Professor Chris Rogan, for his constant dedication to this analysis, his seemingly endless insight into physics, and the indefatigable mentorship and guidance he provides his graduate students. This analysis would not have existed without his tireless efforts and willingness to always offer an explanation, no matter how trivial the concept. Thank you for always letting me bother you with my myriad of questions. Secondly, I would like to thank my committee members, Professors Alice Bean and KC Kong. Alice has been a wonderful informal mentor to me and countless other students during her time at KU. She has been a driving force behind the experimental HEP group for years and is truly an inspiration to female physicists. KC is the most patient professor I have ever met; he is more than willing—in fact, eager—to discuss group theory, complex analysis, or any other complicated topic with his students, both in and out of the classroom. These two professors have been integral to my time so far at KU and I am grateful to them for being on my committee. Thirdly, I would like to thank the entire KU experimental HEP group. The professors within this group have a plethora of knowledge that will lead us to produce some very exciting results. The graduate students are the most hard-working group of scientists I have met. I am so excited to see what this group accomplishes in the rest of my time here. Fourthly, I would like to thank the Madison and Lila Self Graduate Fellowship for having funded and professionally supported me for the last three years. The programming I've received through the Fellowship has been life-changing. I would also like to thank the Lowry family for their generous award that made my transition to Lawrence and my first year of graduate school so smooth. Last, but certainly not least,

I would like to thank my family and friends for all the of support through my years of schooling. Thank you to my parents, who have nurtured my passion for science since I could walk. Thank you to my sister, who is always ready to lend an ear. And to my friends across the country: in Chicago, New York, Seattle, Austin, Los Angeles, San Francisco, and—most importantly—here in Lawrence, thank you for always encouraging me to be my nerdiest self.

Contents

List of Figures

List of Tables

Introduction

For the last half century, the Standard Model (SM) has been the prevailing theory of our universe, from Newtonian physics to the quantum realm [1]. Particle physicists have used this model to predict new particles and their interactions, which have been subsequently confirmed by experiment to stunning precision [2]. This theory is able to describe and predict how atoms are held together, the radioactive decays that power nuclear reactors, and the way that sunlight interacts with our eyes. With the confirmation of the existence of the Higgs boson in 2012 [3, 4], the Standard Model may seem complete.

However, this is not the case. There are instances where the Standard Model is lacking. For example, there is a mathematical divergence predicted in the squared mass of the Higgs boson. Experimentalists know that this divergence is not observed, and as such is tenuously resolved through fine-tuning. Searching for a more fundamental, satisfying answer to this problem is one open question in the Standard Model. Another example of the Standard Model's insufficiency is that everyday, baryonic matter is only 5% of the known universe. Dark matter is theorized to make up 25% of our universe, and there is no evidence yet of dark matter directly interacting with SM particles.

Clearly, the Standard Model does not provide a complete picture of our universe. This has encouraged physicists over the past several decades to search for evidence of physics beyond the Standard Model (BSM). There have been a plethora of frameworks to address the open questions in the Standard Model, but few have been as well-motivated as the theory of supersymmetry (SUSY),

which puts forth a relatively intuitive attempt to create a more complete understanding of the universe. While some theories tackle only one of the open questions in the Standard Model, SUSY provides solutions to many. Formulated to address the quantum loop corrections of the Higgs boson mass, SUSY also provides a stable dark matter candidate [5]. Particles within the SUSY framework (known as *sparticles*) should theoretically be able to be detected at current or near-future energies at the LHC. Specifically, the nature of SUSY suggests that these sparticles should have masses close to that of the electroweak scale.

Even though the masses of the SUSY particles should be the same as their SM counterparts, we have yet to observe SUSY particles at SM scales. This has lead particle physicists to believe that SUSY exists in our universe as a broken symmetry, with the masses of the sparticles hypothesized to exist at the TeV scale [5]. This energy scale is able to be probed with particle colliders like the Large Hadron Collider (LHC) [6].

However, searching for SUSY is not without its challenges. At the LHC, many Standard Model processes produce finals states similar to those of SUSY production and decays, making it difficult to discern between signal and background processes. Additionally, there are areas of experimental phase space that are difficult to probe because the mass of the parent sparticle is so close to that of its invisible child sparticle. When these masses are close to each other, it is known as *compression*. In the compressed regime, most of the energy from the parent sparticle goes to producing an on-shell child sparticle, leaving little energy left over for the momentum of this child. Thus, these events results in soft decay products, with most of the parent sparticle energy going towards the invisible child's mass. These low momenta particles can difficult to accurately reconstruct in the Compact Muon Solenoid (CMS) detector [7], whose technology will be discussed in greater detail in Section 1.2.

Despite the challenges of these compressed scenarios, this analysis is specifically designed to target this area of phase space. The Recursive Jigsaw Reconstruction (RJR) method [8, 9] is the main analysis strategy. This method algorithmically extracts information from events at the LHC and is especially useful for events with missing energy from supersymmetric decays. One of

the signatures we look for in this analysis is the presence of *missing transverse energy*, or MET ($\vec{\not{E}}_T$). More accurately, this quantity is the negative vector sum of the transverse momentum of the reconstructed particles in an event. MET could be due to neutrinos, or a BSM particle that is stable and does not interact with SM matter, which is why we want to focus on events with MET in this analysis.

The underlying idea of RJR is to use the various rest frames and the associated boosts within an event to focus in on the missing energy, information that escapes the CMS experiment without detection. The mechanics of this method are explored in more depth in Section 2.1. The analysis uses two main RJR kinematic variables, R_{ISR} and $M_{\perp}$, with some auxiliary variables and physics object categorization as well.

While we have to account for the Standard Model background in our analysis, we also have to estimate how much of the overall background comes from particles that the detector either mismeasured or misfired on, leading to "fake" physics objects in our reconstruction. One such source of fake background comes in the form of fake leptons. In this analysis, fake leptons are defined as "non-prompt" electrons or muons, not originating from the decay of a W/Z boson, photon, or heavy SUSY particle, and other physics objects that were misidentified as leptons. The nature of fake leptons is examined in more detail in Section 3.

Because the physics of this background is different from other, "prompt" SM processes, fake backgrounds must be accounted for separately from dominant SM backgrounds. Traditionally, a "fake rate," which is the probability of a fake lepton to pass the prompt lepton selection, is measured in a fake enriched region of phase space, which is a region where we expect to see lots of non-prompt and misidentified leptons. This fake rate is then extrapolated from this control region to the region of interest, where the signal would appear. Despite the ubiquitous use of this method in high energy physics analyses, this fake rate method typically does not take into account how the physics behind these fake processes could potentially alter the "shape" of the data, or how the events are distributed. By imposing simulated variations on template shapes, our analysis is able to account for changes in the shape of the data due to fake leptons. The traditional fake lepton

estimation method and our novel shape-based method are both elaborated on in Sections 3.2 and 3.3 respectively. Finally, preliminary results for the overall analysis as well as the results of the additional fit systematics are presented in Section 4. Before continuing into the details of this particular analysis, we begin with some theoretical motivations for SUSY.

1.1 Supersymmetry and its motivation

Part of what makes SUSY such an attractive theory is that it resolves to many of the Standard Model's open questions, like a candidate for the mystery of dark matter. One of the insufficiencies of the SM that SUSY resolves is the quantum loop corrections to the squared mass of the Higgs boson. Because the Higgs boson couples to all SM particles to provide them with mass, these particles appear virtually in Higgs self-couplings. Examples of these couplings can be seen in Figure 1.1, where the right figure shows a Higgs coupling to a fermion and the left shows the same for a superpartner of an SM fermion.

Each of the terms contributing to the quadratic divergence of the Higgs mass is proportional to the squared coupling constant, λ^2, and the ultraviolet momentum cutoff, Λ_{UV}. This cutoff, used to regulate the loop integral of Feynman diagrams (such as those in Figure 1.1) as an upper bound, can be interpreted as the lowest energy scale at which new physics would enter. There are contributions from bosons as well as fermions to the Higgs squared mass. Both of these types of terms are shown in Equation 1.1.1, with the λ_f terms corresponding to the fermionic contribution (Figure 1.1 left) and the λ_S terms corresponding to the bosonic contributions (Figure 1.1 right). These contributions

Figure 1.1: Quantum loop corrections to the Higgs boson with a fermion f (right) and scalar sparticle S (left). [5]

are proportional to the squared masses of their corresponding particle mass, m^2. Since the top quark is the heaviest SM particle, its squared mass provides the largest contribution to these corrections.

$$\Delta m_H^2 = -\frac{|\lambda_f|^2}{8\pi^2}\Lambda_{\mathrm{UV}}^2 + \cdots + \frac{\lambda_S}{16\pi^2}\left[\Lambda_{\mathrm{UV}}^2 - 2m_S^2 \ln(\Lambda_{\mathrm{UV}} m_S) + \ldots\right] \tag{1.1.1}$$

If Λ_{UV} is around the scale of the Planck mass, $M_P = (8\pi G_{\mathrm{Newton}})^{-1/2} = 2.4 \times 10^{18}$ GeV, that means that these corrections are more than 30 orders of magnitude larger than the squared mass value given from the experimentally obtained value of $m_H = \sqrt{2\lambda v^2} = 125$ GeV. Known as the *hierarchy problem*, this discrepancy in scale between the Higgs mass and Planck mass is tenuously resolved through fine-tuning in the Standard Model. This fine-tuning is the process through which the parameters in the Standard Model are adjusted to match to observation [5]. Still, particle physicists have been striving for a more satisfying explanation for this discrepancy.

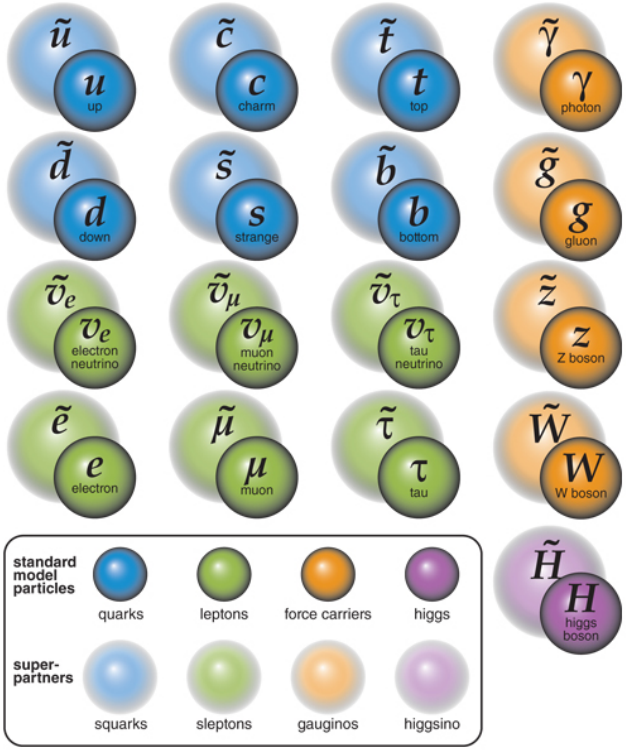

Figure 1.2: Standard Model particles with their supersymmetric counterparts. Credit: Barbara Aulicino

Supersymmetry (SUSY) [5] offers a potential solution to the hierarchy problem. This theory

relates the two types of particles in the Standard Model, fermions and bosons, through superpartners of the opposite type. A supersymmetric transformation turns an integer spin boson into a half-integer spin fermion, and vice versa. The naming convention is that a SM fermion's (f) superpartner is a *sfermion* ($\tilde{f}$), and the superpartner of a gauge boson (V) is a *gaugino* ($\tilde{V}$). The Minimal Supersymmetric Standard Model (MSSM) consists of the same $\mathrm{SU}(3) \times \mathrm{SU}(2) \times \mathrm{SU}(1)$ symmetry of the Standard Model, in addition to its eponynous supersymmetry, the transformation that takes fermions to bosons and vice versa. This theory also features a Higgs doublet to ensure the cancellation of the quadratic divergent terms and to provide mass to both kinds of charged fermions within a generation [1]. The supersymmetric particles can be seen with their SM counterparts in Figure 1.2.

Extending the symmetries of the SM in this way would predict the MSSM superpartners to have the same masses as their SM counterparts, if SUSY was an unbroken symmetry. This means that evidence for SUSY would have been found long ago with masses as light as $m_{\tilde{e}} = m_e = 0.511$ MeV. This mass inconsistency suggests that SUSY is a broken symmetry at the scale we are currently able to probe. Even if the masses between superpartners are not degenerate, the dimensionless coupling constants between scalar and fermionic particles must still be related to avoid the quadratic divergences that we are trying to cancel. Thus, the supersymmetric Lagrangian can be written as the linear combination of two terms: $\mathscr{L}_{\mathrm{SUSY}}$, a supersymmetrically invariant term which carries all of the gauge and Yukawa interactions, and $\mathscr{L}_{\mathrm{soft}}$, which violates supersymmetry with nondegenerate mass terms and coupling constants with a positive mass dimension [5].

The terms in the SUSY Lagrangian that contribute to the breaking of this symmetry become negligible at energy scales higher than those of the SUSY particle masses. It follows to assume that the scale of SUSY breaking is tied to the scale of electroweak symmetry breaking, stabilizing the gauge hierarchy and providing a coherent interpretation for why the electroweak energy scale is so much lower than the Planck scale [1]. This soft supersymmetry breaking implies that masses of superpartners should exist at around the TeV energy scale to avoid the fine tuning currently in the SM to bring these energy scales into agreement. In other words, SUSY at the electroweak scale

is well motivated because the terms that contribute the most to the Higgs corrections are due to heavier fermions, whose superpartners' masses should be close to their SM counterparts (around the TeV level).

In addition to addressing the Higgs quantum corrections, SUSY also provides a candidate for dark matter, which comprises 25% of the known universe and remains unaccounted for in the Standard Model [1]. In R-parity conserving SUSY, the lightest supersymmetric particle (LSP) must be stable. The R-parity of a particle is defined as $(-1)^3(B-L)+2s$, where B is the baryon number, L is the lepton number, and s is the spin. Supersymmetric particles have an R-parity value of -1, which means that in R-parity conserving models, each sparticle must decay into a final state that contains an odd number of LSPs, with the LSP being a stable SUSY particle that does not decay [5]. In line with cosmological constraints, the LSP must be electrically and color neutral—and weakly interacting with SM matter—potentially showing up in detectors in the form of missing momenta [1]. These features make the LSP a promising candidate for dark matter.

Another SM discrepancy that the MSSM addresses is force unification. Already within the SM, two of the fundamental forces, the electromagnetic and the weak force, are unified at probeable energy scales. Extending the SM into the MSSM allows for the unification of the three gauge couplings at an energy scale of around $M_U \approx 3 \times 10^{16}$ GeV [10].

This analysis specifically targets a wide range of R-parity conserving MSSM models, which provide a stable dark matter candidate in the form of the lightest supersymmetric particle (LSP). These types of models also enforce pair production of sparticles. For the scope of this paper, we will focus on interpretations in the form of electroweakino pair production (the TChiWZ model, Figure 1.3).

Clearly, supersymmetry is a highly motivated theory with potentially paradigm-shifting implications. However, searching for SUSY in the electroweak sector, while well motivated by SM masses, is difficult in part due to the fact that sparticles have small production cross-sections meaning that if they are produced at the LHC, they are not produced very often. Additionally, the phase space to search within is quite large, with many combinations of superpartner masses, decays, and

couplings available to be experimentally tested. One area of this phase space that has been notoriously difficult to probe is the compressed sector, where the mass of the parent sparticle is very close to that of the LSP. For example a compressed electroweakino pair production, demonstrated in in Figure 1.3, would mean that the mass of the intermediate (parent) stop particle, $m_{\tilde{\chi}_1^0}$, is close to that of the LSP, $m_{\tilde{\chi}_1^0}$, such that the visible decay products (any leptons or b-jets originating from the top quark) would have little to no momentum. Compression could also occur in certain signal processes that include top quarks where the mass splitting is close to that of the top mass. These compressed decays can lead to off-shell bosons and tops, and ultimately soft final state particles, which are challenging to reconstruct in detectors at the LHC.

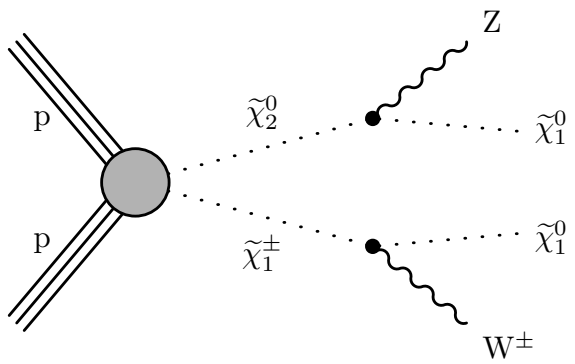

Figure 1.3: The Feynman diagram for the electroweakino pair production (TChiWZ) process considered in this paper.

1.2 The Large Hadron Collider and Compact Muon Solenoid Detector

The Large Hadron Collider (LHC) is a 27 kilometer circumference ring located in Geneva, Switzerland. Within this ring, packets of protons are accelerated to nearly the speed of light, controlled by magnets and radiofrequency cavities, with a current collision center of mass energy of 13 TeV [6]. These packets of protons collide at certain points around the accelerator within experiments known as detectors. Currently, the collision rate at the LHC is 40 MHz, or proton collisions every 25 nanoseconds. Only a fraction of this data is actually recorded though. Since there is so much data produced at the collider, we employ a system of triggers to only record certain, interesting

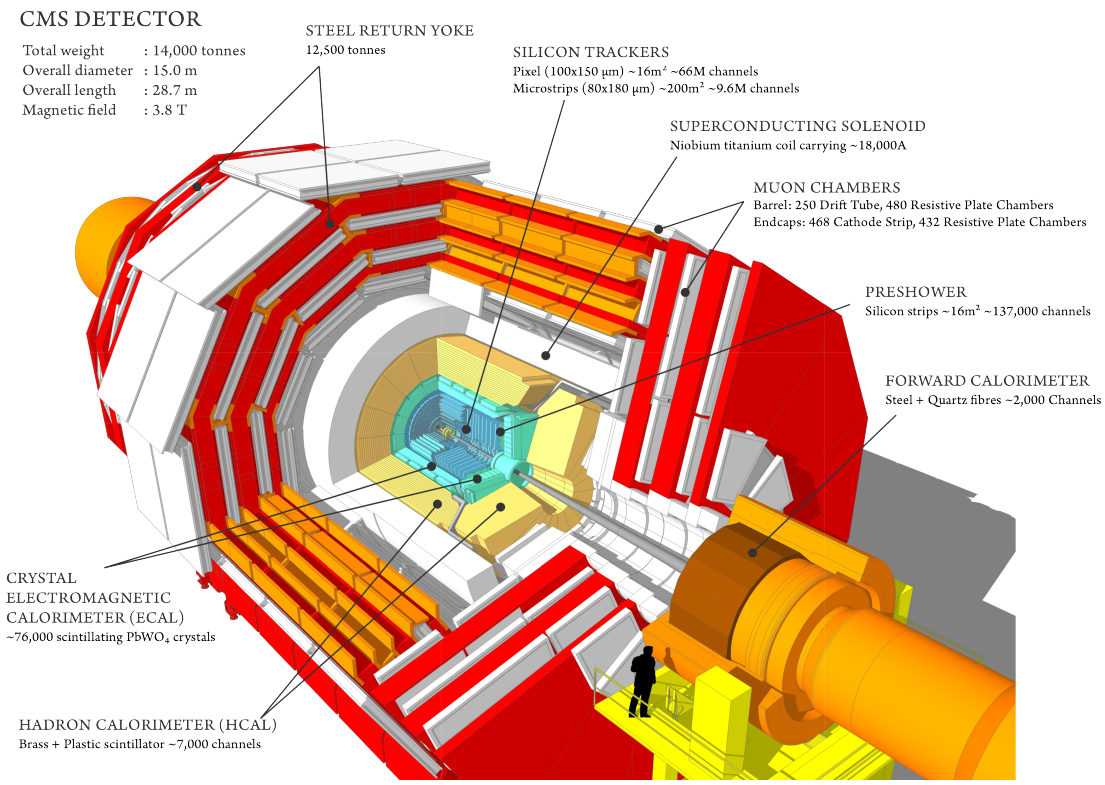

Figure 1.4: Sliced view of the CMS detector.

events. At the Level-1 trigger, data are recorded at a rate of 100 KHz. This rate is further reduced with the High Level Trigger to 1 KHz.

There are several experiments at the LHC, and one of the general purpose detectors is the Compact Muon Solenoid (CMS) detector. This detector is comprised of five main layers, each with a specific technology to measure different aspects of a collider event [7]. The different layers of the CMS detector can be seen in Figure 1.4.

The innermost part of the CMS detector is the tracking layer. The CMS tracker is comprised of silicon pixel detectors closest to the collision, or interaction point, and silicon strip trackers further away. The particles that come from the collision, or from decays of heavier particles produced in the collision, leave tracks in this layer. The next layer is the electromagnetic calorimeter (ECAL), which measures energy deposits from charged particles. This is a hermetic calorimeter, meaning it covers the entire range of the azimuthal angle, $-\pi \leq \phi \leq \pi$, and the pseudorapidity up to 3 ($|\eta| < 3$) [7]. It is also homogenous, which means it is made of one solid material, lead tungstate,

that is separated into about 70,000 crystals. Generally, electromagnetic particles like electrons and photons are stopped by this layer. The hadron calorimeter, surrounding the ECAL, measures energy deposits from hadrons. Unlike the ECAL, the hadron calorimeter is a sampling calorimeter. It has alternating layers of copper absorber plates and plastic scintillator tiles [11].

Surrounding the hadronic calorimeter is the CMS's eponymous solenoid, a superconducting magnet with a field strength of about 3.8 Tesla. A charged particle's path curves in a magnetic field, and the amount of curvature is proportional to the magnetic field strength and to the particle's momentum. Since particles produced at the LHC have relatively high momentum, we need a strong magnetic field to curve their trajectory enough to be measurable. Since this curvature depends on the particle's momentum and electric charge, we can use the curvature under the solenoid to help identify particles and measure their momenta. The momentum component of particles produced at the LHC that we are often interested in is the *transverse* momenta, p_T. Following the beam line down the orange tube in Figure 1.4, p_T is the momentum component transverse to this axis. This quantity is longitudinally invariant, and therefore conserved in the proton collisions that CMS measures, which means that from this quantity, we are able to calculate missing transverse energy.

Finally, the outermost layer of the CMS detector is the muon chambers. Muons are similar to electrons, except that they are about 200 times heavier and are only stable for a fraction of a second. They are generally not stopped by the previous layers of the detector, so in order to gain more information about these particles there is a specialized detector subsystem for them at the edge of CMS. The muon chambers are comprised of drift chambers in the central, barrel area of the detector and cathode strip chambers in the endcap sections [12]. Both technologies in the muon chamber are electronics in a gas, such that when muons pass through, they ionize the gas and this interaction can be read out as an electrical signal.

Particle physicists combine the information, read out as electrical signals as particles pass through the detector, from all of the CMS layers to reconstruct the particles produced in collisions. Since supersymmetric particles do not interact with the detector material, like SM particles do, we need to consider additional techniques for these sparticles. One way to increase our probability

of observing sparticles is to increase the energy of the collisions to potentially produce heavier sparticles.

With recent advancements in technology at the Large Hadron Collider, we have been able to achieve center-of-mass collision energies of 13 TeV for proton-proton collisions, which has brought us closer to potentially observing sparticles at the TeV scale. For this analysis, we are working with data from Run II of the LHC with an integrated luminosity of 137 fb^{-1}. For the scope of this paper we analyze the three years of Run II (2016-2018) separately, each year comprising about a third of the total integrated luminosity.

If we wanted to increase our chances of observing new physics, increasing the collision energy would give us insight into higher particle masses and shorter length scales. Alternatively, we can crank up the instantaneous luminosity of the LHC to increase the probability of observing these rare supersymmetric processes. Such an increase in the collision rate is exactly what physicists are currently working towards to achieve approximately 5 to 7 times more instantaneous luminosity. Upgrades to bring the LHC into its high luminosity (HL) era are currently underway, with the first HL-LHC run tentatively scheduled for the mid-2020's. While we work towards the HL-LHC, we can look at data from previous runs and events simulated from Monte Carlo (MC) methods. In the MC simulations, events are simulated with the event generator, then run through a detector simulator to approximate the reconstruction effects we expect to see. These simulated events are used as central, or expected, values for event yields. MC events are used to design the analysis, specifically in defining the analysis regions, which are described in Section 2.

Analysis Strategy

2.1 Recursive Jigsaw Reconstruction

We reconstruct events in the analysis described in this paper using Recursive Jigsaw Reconstruction (RJR) [8, 9]. This method exploits the compression between the masses of the parent and child sparticles to discriminate signal SUSY processes with massive sparticles from background SM processes. RJR iterates through approximations of the rest frames of the event by making algorithmic choices at each step. An example of a set of these rest frames can be seen in Figure 2.1. Here, we can start in the lab frame, where the particles' 4-vectors are measured, at the top of the diagram and apply choices to approximate the boost to the center-of-mass (CM) frame, then to the sparticle (S) rest frame, finally decomposing that into visible (V) and invisible (I) decay products. In this particular analysis, we also account for the presence of an initial state radiation (ISR) system, which will be elaborated on later in this section.

These algorithmic choices are known as the *jigsaw rules*, because they are factorizable, customizable, and interchangeable, and they are *recursively* applied on the event to reconstruct observables. From the application of these jigsaw rules, RJR produces a basis of kinematic observables to study, that all provide largely independent information. These observables are specifically formulated to be sensitive to a massive invisible particle, separating these events from SM background, which could potentially contain missing energy in the form of the virtually massless neutrino.

These RJR rules are enforced to minimize a kinematic quantity of interest such that we can

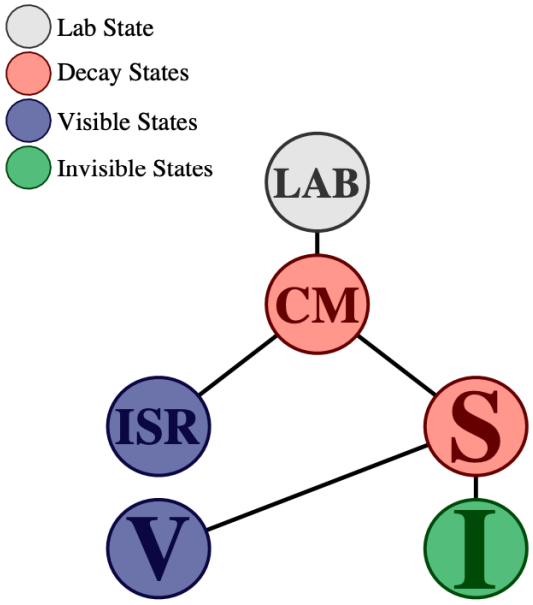

Figure 2.1: A generic RJR decay tree for analyzing compressed signal events, where each vertical level is a different reference frame [9].

constrain a degree of freedom for the invisible particle. The choice to minimize, rather than maximize, a certain kinematic quantity (usually masses or energies) comes from the error in our choice of boost $\vec{\beta}_{\text{CM}}^{\text{lab}}$ from the lab frame to the center-of-mass frame for the system. Both over-boosting ($\vec{\beta} > \vec{\beta}_{\text{CM}}^{\text{lab}}$) and under-boosting ($\vec{\beta} < \vec{\beta}_{\text{CM}}^{\text{lab}}$) can overestimate the mass/energy describing the center-of-mass system. For example, incorrectly assuming the invisible particle(s) in the decay are massless could lead to an overboost of the sparticle system. Thus, minimizing the chosen kinematic quantity for the center-of-mass frame will get the boost as close as possible to its true value, allowing for an approximate transfer to the center-of-mass frame from the lab frame.

RJR is especially helpful in the compressed regime this analysis is targeting. In compressed scenarios, the final state particles would receive little to no momentum from their parent decays, barely being produced on-shell. In order to more accurately reconstruct these final states and maximally obtain information from the event, we would like the system with the supersymmetric particles to recoil against a system of jets from ISR. This recoil gives the soft decay products some momentum, providing a boost from the lab frame where the proton-proton collision happens, to the center-of-mass frame, where the momenta of the ISR system and the sparticle system are balanced.

Here, the sparticle system decays to a final state with a visible system (i.e. leptons or jets) and an invisible system (i.e. neutrinos or LSPs). As we will see in section 2.2, we can derive kinematic variables from this method of analyzing events that strongly discriminate between signal processes with massive invisible particles and background with massless ones.

The principle discriminating variables are R_{ISR} and $M_{\perp}$, which are sensitive to orthogonal relationships of sparticle masses. Qualitative derivations of these observables, as well as intuition behind the discriminating power of these variables, are given in Section 2.2. Because of the general nature of these observables, a variety of supersymmetric models are considered as viable interpretations in this analysis, specifically within the simplified model spectra (SMS). For the scope of this paper, we focus on electroweak pair production, whose Feynman diagram can be seen in Figure 1.3.

2.2 Kinematic observables

The observables in this analysis are designed to be sensitive to a massive LSP, which would show up in the CMS as missing transverse momentum ($\vec{\not{E}}_T$), which is the negative vector sum of the momentum transverse to the beam line. In the CMS detector, we are not able to obtain information about the masses from $\vec{\not{E}}_T$, since it only represents the sum of the momenta of undetected particles. For SM backgrounds, this is not an issue because physical missing energy is largely due to neutrinos, which have negligible masses. However, for massive supersymmetric particles, this is not the case. If we are able to boost from the observed lab frame to an approximation of the production frame of the final state (rest frame of the intermediate sparticle), this boost would give us information about the mass of the LSP. In the limit of compressed scenarios, the missing energy of an event can be approximated as

$$\vec{\not{E}}_T \sim -\vec{p}_T^{\,ISR} \times \frac{m_{\tilde{\chi}_1^0}}{m_{\tilde{p}}} \,, \tag{2.2.1}$$

where $\frac{m_{\tilde{\chi}_1^0}}{m_{\tilde{p}}}$ is the ratio of the LSP mass to its parent mass. With the RJR technique, we are able

to assign physics objects in the event to the branches in the Figure 2.1 decay tree and, as such, extract the relevant kinematic quantities for each system.

To be sensitive to the mass ratio with the sparticle system, we can use the kinematic variable R_{ISR}, defined below, to approximate the ratio of the LSP mass to the parent mass.

$$R_{ISR} = \frac{|\vec{p}_{I,T}^{\,CM} \cdot \hat{p}_{ISR,T}^{\,CM}|}{\vec{p}_{ISR,T}^{\,CM}} \,. \tag{2.2.2}$$

We expect this kinematic quantity to peak around the ratio of the child and parent sparticle masses. This peak can be seen in the right plot of 2.2, which demonstrates 2D distributions of R_{ISR} vs. $p_{\mathrm{T}}^{\mathrm{ISR}}$ for signal (with background to the left for comparison). It should be noted that $\hat{p}_{ISR,T}^{\,CM}$ (the direction of the ISR transverse momentum in the center-of-mass frame) is actually the direction of the boost $\vec{\beta}_{\mathrm{CM}}^{\,\mathrm{lab}}$ that takes us from the lab frame to the center-of-mass frame. In this convention, transverse means transverse to the direction of boost axis from the lab frame to our current frame.

This observable is a powerful discriminator between signal and background because it depends on the boost axis direction. Thus, it contains information about any correlations in the decay angle induced by incorrect boosts, where the decay angle is the angle between the visible system and the boost. Since the magnitude of the boost is inversely proportional to the energy of the sparticle system, incorrectly assuming a massless invisible sparticle in the reconstruction will result in an over-boost, and therefore introduces a correlation in our basis of observables for SM backgrounds with massless invisible particles. So, not only do we expect the R_{ISR} resolution to improve for smaller mass splittings, there should also be a correlation in the background for this variable and $p_{\mathrm{T}}^{\mathrm{ISR}}$, or the magnitude of the boost. This is exactly what we see for the background distribution (Figure 2.2a). A similar correlation is present in the slightly compressed signal distribution (Figure 2.2b), but is not as strong as it is in the background case. There also is a slight peak where we expect for this mass splitting, $\frac{m_{\tilde{\chi}_1^0}}{m_{\tilde{t}}} = \frac{400}{350} = 0.875$. In more compressed scenarios, this peak becomes more defined and moves closer to 1 in R_{ISR}.

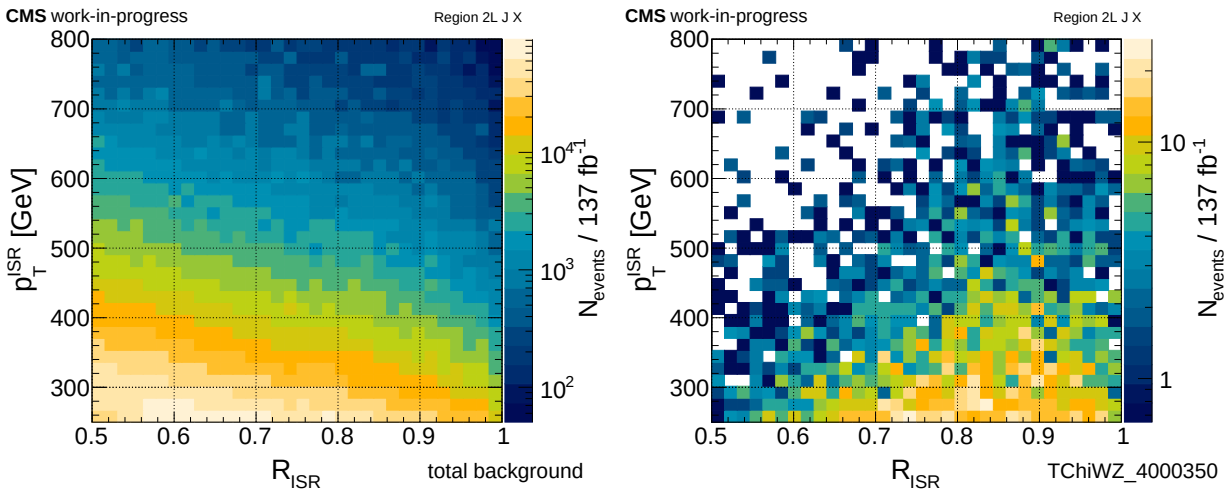

(a) Total background.

(b) TChiWZ signal with $\Delta m = 50$ GeV.

Figure 2.2: 2 dimensional R_{ISR} vs. $p_{\mathrm{T}}^{\mathrm{ISR}}$ distribution for example background (left) and signal (right) in the 2 lepton channel for 2017 Monte Carlo scaled to 137 fb^{-1}.

The other main kinematic variable in this analysis is a mass-dependent variable that is derived specifically for events with pair produced sparticles, which are a feature of R-parity conserving SUSY. Following similar RJR rules, we would want to minimize a kinematic quantity to approximate the boosts between rest frames. In the case of pair production, the kinematic quantity we would want to minimize is not the invariant mass of the intermediate particle (which is not resonant), but rather the sum of masses squared for the pair produced particles. An example of this pair production RJR decay tree can be seen in Figure 2.3. This quantity in question depends on the momenta of the invisible decay particles, which cannot be resolved into the individual particles. Choosing these momenta is another example of a jigsaw rule. In this case, instead of choosing a rule to get us from the lab to the rest frame of an intermediate particle, we are boosting to the production frame of the two pair produced particles. For this jigsaw rule, we want to minimize the total energy of the visible system (the W and Z boson final decay products in Figure 2.3) in the pair production frame with respect to the boost that got us there. Essentially, this is like ignoring our incorrect boost to get us to a frame where the momenta of the visible objects (in this case reconstructed leptons) are balanced. We call this process of projecting out the momenta components parallel to the boost *perpendicularizing*.

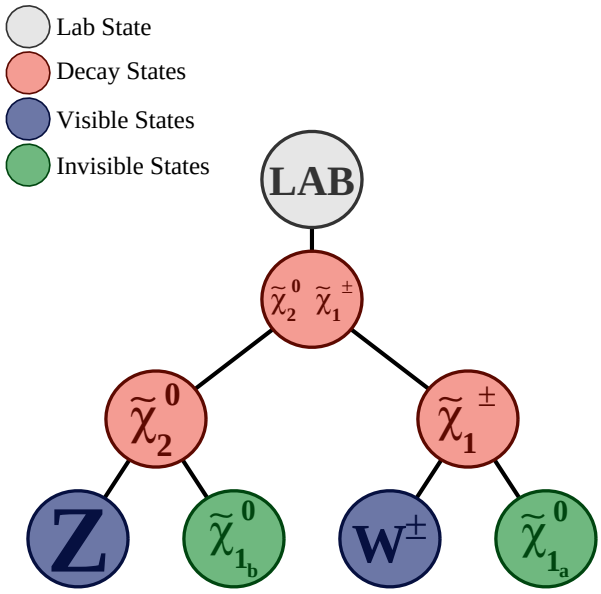

Figure 2.3: An RJR decay tree of the TChiWZ model, demonstrating hemispheres a and b [8].

Once in this frame, we can calculate the sum of the squared masses of the intermediate decay particles to create our second main kinematic variable, $M_\perp$, defined below. In Figure 2.3, the two electroweakinos are the pair produced particles S_a and S_b in Equation 2.2.3.

$$M_\perp = \sqrt{\frac{m_{Sa\perp}^2 + m_{Sb\perp}^2}{2}}\,, \tag{2.2.3}$$

where the squared masses of either sparticle in hemisphere a or b is from a perpendicularized 4-vector. Similar to R_{ISR}, this kinematic variable is sensitive to the absolute mass of the invisible sparticles. However, instead of being sensitive to a ratio of masses, this variable is sensitive to the mass difference between the parent and child particles, such that $M_\perp \sim m_{\tilde{\chi}_1^0} - m_{\tilde{P}}$. This additional variable, which is linearly independent from R_{ISR} for signal approximation, provides another handle on the discrimination between signal and background processes. 2D plots for $M_\perp$ vs. $\gamma_\perp$ (or γ_T, an auxiliary variable which will be described later) for background (top) and signal (bottom) can be seen in Figure 2.4.

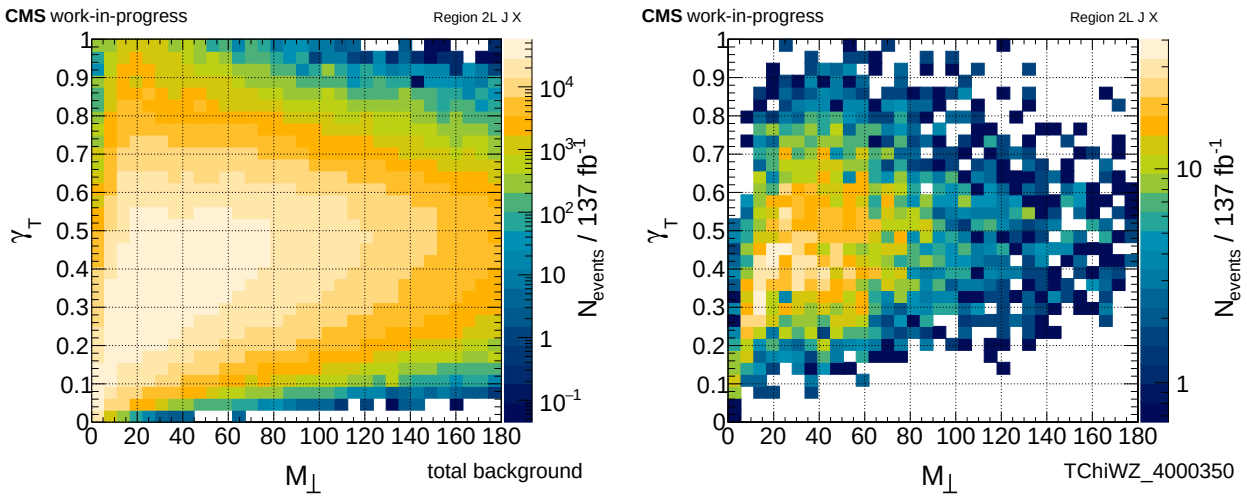

(a) Total background.

(b) TChiWZ signal with $\Delta m = 50$ GeV.

Figure 2.4: 2 dimensional $M_\perp$ vs. γ_T distribution for example background (left) and signal (right) in the 2 lepton channel for 2017 Monte Carlo scaled to 137 fb^{-1}.

While these two main kinematic quantities provide a strong basis to analyze events, we introduce complementary variables to further refine the discrimination between signal and background. Each of these complementary variables can be thought of as paired with a main discriminating variable. For R_{ISR}, this variable is nicely complemented by the transverse momentum of the ISR system that gives the sparticle system a kick, p_T^{ISR}. The resolution of R_{ISR} improves with an increase in boost magnitude, p_T^{ISR}, for signal but not for background, as shown in Figure 2.2 for the signal processes. The rates for signal events also drop off more slowly with a p_T^{ISR} cut than for background. Doing a coarse cut on the complementary variable can help us zero in on areas of phase space that have a high signal to background ratio.

A variable that is complementary to the second main variable, $M_\perp$, is

$$\gamma_T = 2\frac{M_\perp}{m_{S\perp}}\,, \tag{2.2.4}$$

which can be interpreted as the approximate inverse Lorentz factor associated with the boost from the pair production frame to individual sparticle frames. Here, $m_{S\perp}$ corresponds to the perpendicularized mass of the pair produced electroweakino system in Figure 2.3. This kinematic quantity

probes the ratio of the reconstructed invisible child sparticle masses relative to the invariant mass of the pair produced, parent sparticle system. This ratio increases as the invariant mass for the sparticle frame, m_S, decreases, meaning that the visible particles are flying closer together. Consequently, if the visible particles are back to back in the sparticle frame, γ_T is at a minimum. For background processes, this variable peaks in a strongly correlated way at low $M_\perp$ values, seen in Figure 2.4a. The discriminatory power of this variable, like for p_T^{ISR}, is not as great as for our main kinematic variables. From Figure 2.4, we see that the rate of background events falls off more quickly with higher γ_T than it does for the signal distributions. Thus, a coarse cut on γ_T can separate background events at low $M_\perp$, paving the way to see compressed signals more clearly, and to define strong control regions.

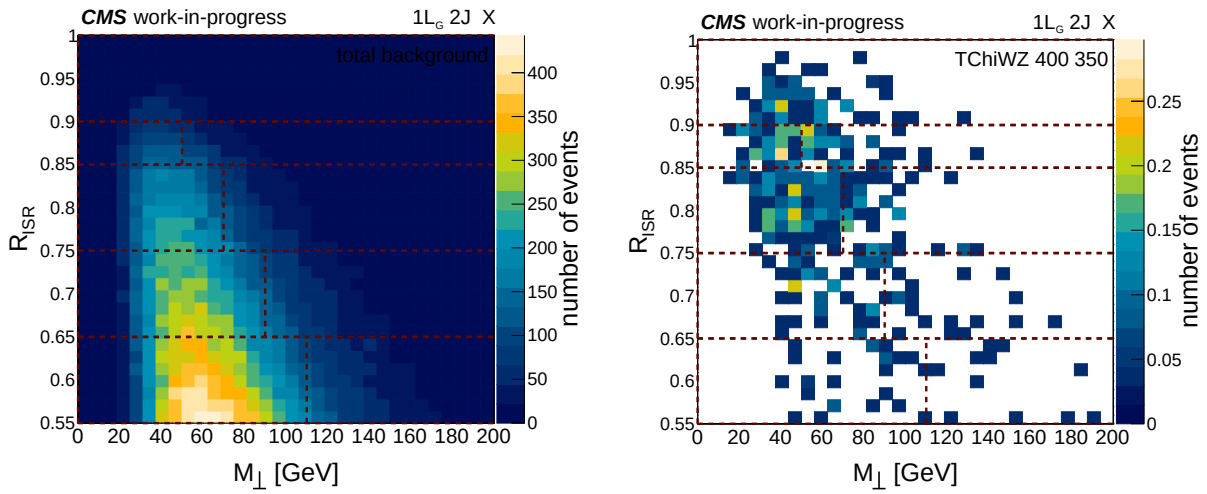

(a) Total background.

(b) TChiWZ signal with $m_{\tilde{\chi}_1^\pm} = 400$ GeV and $m_{\tilde{\chi}_1^0} = 350$ GeV.

Figure 2.5: R_{ISR} vs. $M_\perp$ 2D distribution for all backgrounds and a single signal process mass point with 1 gold lepton and 2 jets in the sparticle system.

This analysis is binned in R_{ISR} vs. $M_\perp$, creating two dimensional distributions of events, as seen in Figure 2.5, with bins in the discriminating variables shown with the dotted lines. These 2D histograms can be "unrolled" into one dimensional histograms to better view the actual shape of the distributions. Figure 2.6 shows an example of these 1D distributions, with the bracketed bins

showing the R_{ISR} bins, the vertical black lines separating the $M_{\perp}$ bins and further physics object categorizations labeled at the top of the bins (including number of b-jets and secondary vertices in the sparticle (S) and ISR (I) systems.

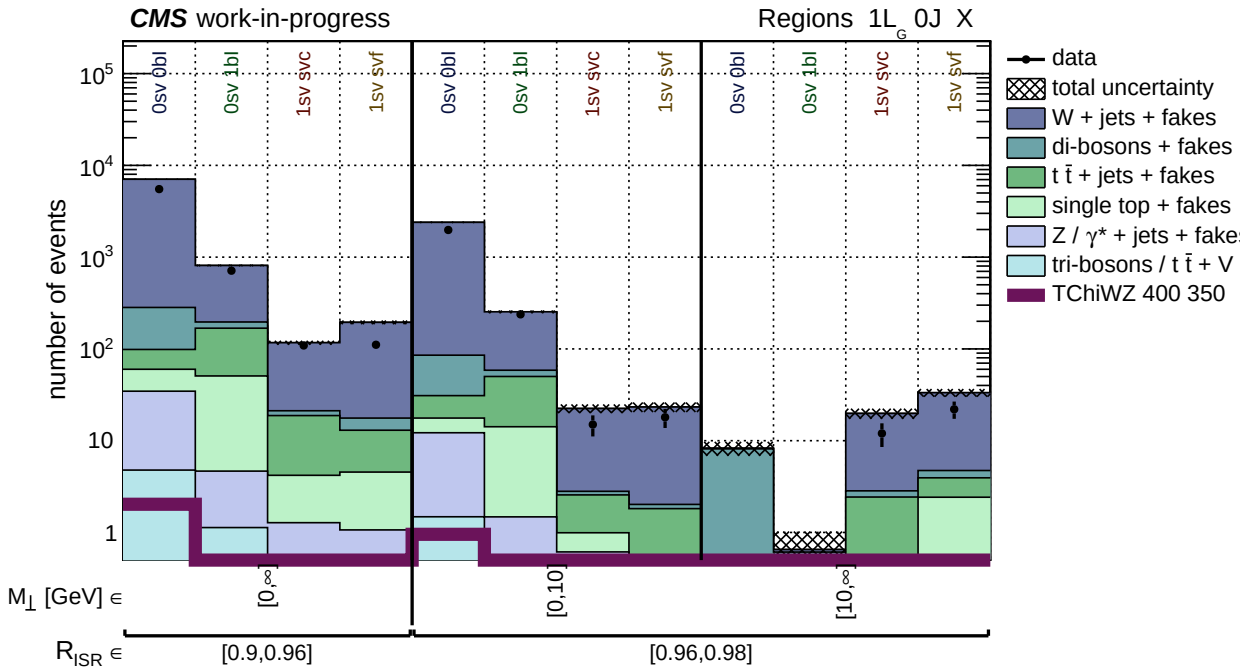

Figure 2.6: R_{ISR} and $M_{\perp}$ 1D control region distributions for all backgrounds, data, and one TChiWZ mass point with 1 gold lepton and 0 jets in the sparticle system in 2017.

2.3 Lepton categorization

Because this analysis targets a variety of signal models with different final states, this analysis also separates events by object count, quality, and combinatoric decay tree assignment. Despite the main SM backgrounds decaying to final states that are similar to those of our signal processes (Table 2.1), we can exploit the discriminating power of our main kinematic variables and physics object categorization to separate background and signal events.

Background process	Possible final state
$t\bar{t}$	b-jets, leptons, missing energy
W+jets	jets, leptons, missing energy
Z/Drell-Yan	jets, leptons or missing energy

Table 2.1: How final states for main background processes could imitate signal final states.

The channels of this analysis are 0, 1, 2, and 3 leptons. Reconstructed leptons are qualified by a mutually exclusive analysis-specific ID: “gold," “silver," and “bronze". The analysis-specific ID requirements are enumerated in Table 2.2 and Table 2.3, where the Tight and Medium IDs are CMS specific definitions for electrons [13] and muons [14].

	Gold	Silver	Bronze
Tight ID	pass	pass	fail
$\mathrm{IP_{3D}}/\sigma_{\mathrm{IP_{3D}}}$	< 2	≥ 2	≥ 2
$\mathrm{PFIso_{abs}}$ or $\mathrm{MiniIso_{abs}}$	< 4 GeV	< 4 GeV	≥ 4 GeV

Table 2.2: ID requirements for electrons.

	Gold	Silver	Bronze
Medium ID	pass	pass	fail
$\mathrm{IP_{3D}}/\sigma_{\mathrm{IP_{3D}}}$	< 2	≥ 2	≥ 2
$\mathrm{PFIso_{abs}}$ or $\mathrm{MiniIso_{abs}}$	< 4 GeV	< 4 GeV	≥ 4 GeV

Table 2.3: ID requirements for muons.

These IDs are representative of three kinds of leptons we expect to see in this analysis. The gold ID is reserved for the highest quality leptons; these are the most signal-like, most likely to be a direct product of a SM boson or BSM particle by the cut on the 3D impact parameter ($\mathrm{IP_{3D}}$), significance of this parameter $\mathrm{IP_{3D}}/\sigma_{\mathrm{IP_{3D}}}$, and its isolation, which is a measure of detector activity in a given area around the particle. The silver ID, orthogonal to gold and bronze IDs, is for

recovering efficiency from leptons in semi-leptonic b decays or tau decays. These are considered isolated, but not prompt. Finally, the rest of the leptons in this analysis are categorized within the bronze ID, the so-called “fakable object" ID. We expect this category to catch a majority of our fake leptons.

In addition to considering lepton quality and multiplicity, this analysis is also categorized by the number of reconstructed jets, b-jets, and secondary vertices (SVs) in the event. B-jets are identified by two neural networks: the standard CMS DeepJet algorithm [15] and a new tagger, specifically designed to tag soft b-jets using secondary vertices as inputs [16]. Furthermore, the categories are expanded upon by where each of the objects in the event are assigned in the RJR decay tree, either within the sparticle system (further separated into the a and b hemispheres for pair production) or the ISR system. An overview of the variables used in this analysis is shown in Table 2.4

Physics Object/Observable	Categorizations
R_{ISR}	distribution binning
$M_{\perp}$	distribution binning
p_T^{ISR}	coarse binning
γ_T	coarse binning
Lepton multiplicity	0, 1, 2, 3
Sparticle jet multiplicity	0, 1, 2, 3, 4, 5+
B-jet or SV multiplicity	0, ≥ 1, ≥ 2
Lepton flavor	μ, e
Lepton quality	bronze, silver, gold

Table 2.4: Analysis binnings and categorizations.

Fake Leptonic Background

3.1 Fake leptonic background processes

Detectors at the LHC are able to identify, or reconstruct, particles that fly out of the collisions to extraordinary precision, especially given the sheer volume of data that is read out every second. However, these detectors are not perfect, and sometimes particles are mis-measured. These particles are known as “fakes." Specifically, fake leptons are a source of background in our analysis. These fake leptons, also known as “non-prompt" leptons, are leptons that are not an immediate decay product of a W/Z boson or a heavy sparticle (such as a slepton, the supersymmetric partner of a lepton). Rather, these non-prompt leptons come from semi-leptonic heavy or light flavor decays. Other types of fake leptons may arise from mis-measurement of charged hadrons, jet punch-through, or misidentified photon conversions. In the CMS detector, these kinds of leptons may appear as muon chamber punch-through, for example. This is where jet activity extends beyond the hadron calorimeter into the muon chambers, thus mimicking the muon signature. At generator level, a fake may also arise from an “unmatched" reconstructed lepton, that is, a reconstructed lepton that could not be matched to a true lepton. Background contributions due to fake leptons are non-negligible in the main analysis backgrounds, including $t\bar{t}$, $W+$jets, and Drell-Yan processes, across the 1+ lepton categories due to the focus in the analysis on low p_T leptons.

3.2 The tight-to-loose method

The usual method of estimating the background contribution from fake leptons is called the “tight-to-loose," or “fake factor," method. The “tight" selection is the signal lepton definition and the “loose” selection is similar, with some looser requirement to ensure that the selection is dominated by fake leptons (so-called “fakable object" selection). This looser requirement is typically on isolation, which is a measure of how many other particles are in a conical area surrounding the lepton in question by calculating the sum of the energy in the cone. This requirement ensures that the tight selection is a subset of the loose selection. The “fake rate" ε_{TL} is then defined as $\frac{N_{tight}^{NP}}{N_{loose}^{NP}}$, which can be interpreted as the probability of a fake lepton to pass the tight identification, given that it has passed the loose selection. This fake rate is measured in some sideband, or “measurement region," which is a region in the analysis that is designed to be dominated by fake leptons. The rate is then applied to the “application region." This region is kinematically similar to the signal region (SR), apart from the leptonic cuts, which satisfy the loose ID. Because it is orthogonal to the SR, the application region is considered a loose-not-tight ($L!T$) selection, usually with a looser isolation selection. The estimated number of fake lepton events in the SR can be extrapolated from the application region via the fake rate,

$$N_{fake}^{SR} = \frac{\varepsilon_{TL}}{1-\varepsilon_{TL}} \cdot (N_{\text{data}}^{L!T} - N_{\text{prompt}}^{L!T}) \,, \tag{3.2.1}$$

where $N_{\text{data}}^{L!T}$ is the data yield in the $L!T$ application region and $N_{\text{prompt}}^{L!T}$ is the prompt Monte-Carlo yield in the L!T application region.

This tight-to-loose method, in data driven and semi-data driven cases, does not take into account shape variations due to fake leptons, only the overall normalization change. The shape of the kinematic distributions could potentially change from fake lepton mis-modeling and we aim to account for this variation in our analysis. The shape for the fake leptonic background is extrapolated from other bins of the signal region. Further, the shape within the discriminating variables could also vary due to lepton flavor, fake source, or other characteristics. The relative normalization of

these discrepancies is taken into account with the fake factor method. For example, to separate the fakes from heavy or light flavor hadron decays, fake factors will be measured separately in b-jet enriched and b-jet depleted regions. However, variations due to these discrepancies are still not accounted for with shape variations, leading us to develop our own fake lepton estimation method that does account for these discrepancies for this analysis.

3.3 A novel shape-based method

The motivation behind this method is that we are trying to capture shape variations in the data due to mis-modeling of fake leptons in simulation. It could be possible that the admixture of fake leptons for a given source is not exactly like that in data, and we would like our fit to be able to potentially resolve this using “sidebands" as control regions. If left unaccounted for, these shape differences could be potentially misinterpreted as signal. Introducing systematic variations into our fit as nuisance parameters allows variations to be constrained directly from data.

From first principles, we expect the yields in adjacent bins in R_{ISR} and $M_{\perp}$ to vary in related ways due to fake leptonic background contributions. We also expect some analysis categories (such as different lepton IDs) to have similar shapes and also behave similarly with fake leptonic background variations. So, for this analysis, we employ a novel shape-based semi-data driven fake estimation method. In this method, we simulate ad-hoc shape variations on top of nominal predictions from simulation. These predicted, central values are one dimensional distributions, like the one previously shown in Figure 2.6. An example of these variations at a maximum of 20% can be seen in Figure 3.1, with the nominal shape (black) corresponding to the normalized 1D histogram. Variations are imposed on top of the unnormalized distribution with the “up" or $+1\sigma$ normalized variations in red and the “down" or -1σ normalized variations in blue.

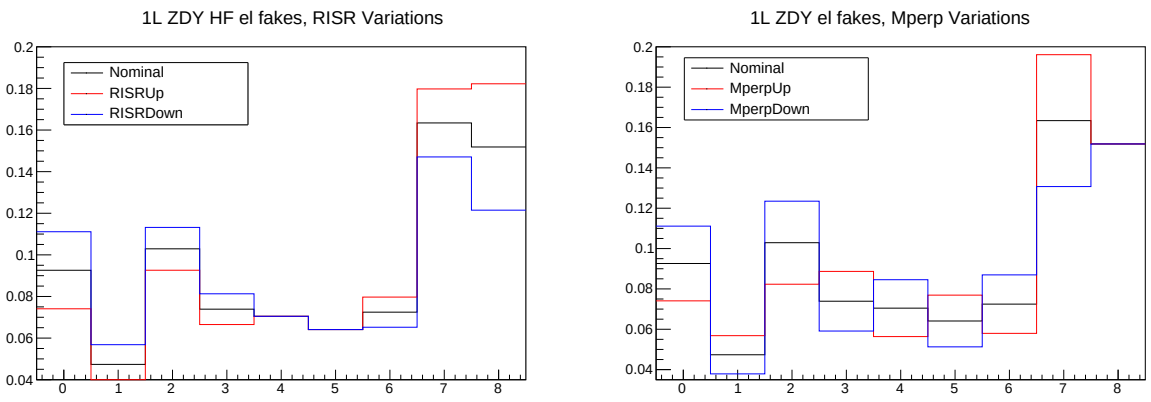

(a) R_{ISR} variations.

(b) $M_{\perp}$ variations.

Figure 3.1: Shape variations imposed on a 1D histogram for Z/Drell-Yan process with one electron that is a heavy flavor fake with 20% maximum variations.

To simulate the variations for the fake lepton shape method, we set a maximum allowed variation for the edge bins in either variable and symmetrically distribute the variations in the intermediate bins such that the middle bin (if it exists) has no relative variation. These variations that are simulated are certain percentages of the normalized histograms, such that the shapes are varied, not the event counts. We simulate variations in shape for each of our discriminating variables, R_{ISR} and $M_{\perp}$, separately such that trends in these observables can be modeled independently. Since the R_{ISR} bins do not repeat (unlike the $M_{\perp}$ bins, which repeat for every R_{ISR} bin), the RISR variations more clearly demonstrate the pattern we impose on both R_{ISR} and $M_{\perp}$. In Figure 3.1a, the maximum variations are seen on the edge bins (bins 0 and 8) and 20% of the normalized bin value. The variations are then distributed evenly among the remaining bins, such that bins 1 and 7 have a 15% variation, bins 2 and 6 have a 10% variation, bins 3 and 5 have a 5% variation and bin 4 has no variation. The same pattern is applied to the variations in $M_{\perp}$. The maximum *a priori* uncertainty, or variation from the central value, for the fake lepton shape variations in the analysis is 5%.

These variations in R_{ISR} and $M_{\perp}$ will act as $\pm 1\sigma$ deviations from the central value shape of the distribution and can be incorporated into our maximum likelihood fit to data as systematic uncertainties in the shape of fake lepton processes [17]. The uncertainties, or model nuisance parameters (NPs), act as extra knobs or degrees of freedom in our fit to better capture any differences

in shape for fake leptons between data and simulation. Rather than attempting to constrain all of the NPs in our model, the addition of these shape uncertainties gives our model this extra “wiggle room" that otherwise wouldn’t exist. These NPs are able to capture shape differences between the reconstructed distributions and the true ones due to fake lepton mis-modeling that either would be potentially mistaken for signal and/or would result in overly-inflated systematic uncertainties, as is the case for the standard tight-to-loose method. The goal of this method is not to constrain every possible NP in our fit, but rather to provide it with informative, physics-motivated degrees of freedom that capture expected systematic effects.

These additional shape systematics, connected across kinematically similar analysis regions, give the fit the freedom to account for these shape differences. The shape comparison studies in Section 3.3.1 detail the quantitative method behind the decision to connect NPs across certain regions. Specifically, the systematics are connected across background processes, lepton IDs, and $p_{\mathrm{T}}^{\mathrm{ISR}}$ and $\gamma_{\perp}$ regions. The systematics are separate for different lepton multiplicities, sparticle system jet multiplicities, fake lepton flavors, and fake lepton sources. Even though some analysis regions are inclusive for lepton flavor, any fake leptons in those regions are still tagged as fake electrons or fake muons, which could enact different mismodeling effects. So, the fake lepton shape systematics are separated out by fake lepton flavor, even in these flavor-integrated regions. A similar shape parameter treatment is also used to help constrain the QCD background in this analysis.

3.3.1 Shape comparison studies

In order to determine which analysis categories should be grouped together for the fake lepton shape systematics described in Section 3.3, quantitative shape comparison studies were performed. These studies used a likelihood test to determine the similarity in shape between two distributions, inspired by the method in a lecture from the 2008 BaBar Analysis School [18]. Usually, the distributions in comparison were the original distribution and a consolidated distribution which includes the original distribution and others that are kinematically similar in the same categorization. We

create consolidated histograms, summing over analysis categories that should behave similarly in terms of fake variations, to serve as the central value on which to impose simulated variations. Ideally, this consolidation procedure will connect the variations of categories that should behave similarly in terms of variations due to fake leptons. This method will also substitute average values for empty bins due to limited Monte Carlo statistics, which is described in Section 3.3.2.

Kinematically, events with a low jet multiplicity in the sparticle system (0 or 1 jets), should behave similarly to each other and different from events with high jet multiplicity (2 or more jets). In the ISR system though, shapes are combined over jet multiplicity for a given sparticle system. Real leptons that are poorly reconstructed or non-prompt will behave differently in the analysis and therefore are separated into the analysis specific IDs (gold, silver, and bronze). Fake leptons, however, should not discriminate between these IDs because they are not produced the same way as real leptons. Therefore, we expect that the shapes between the lepton ID categories for fake leptons should be reasonably similar.

We can calculate the agreement between a histogram and its corresponding consolidated histogram with two metrics: the ratio of the individual histogram to its consolidated counterpart, and the likelihood ratio between these shapes [19]. For the ratio, the histograms in question are normalized independently such that only the differences in shape are studied. In a particular bin, any deviation from 1 (whether greater than or less than) is indicative of a deviation in shape between the original and consolidated histogram. The ratio test gives a qualitative approach to assessing the similarity between shapes. It also provides a method for assessing trends in deviations according to our discriminating variables. However, to quantitatively determine which shapes are in better agreement, a more rigorous approach is necessary.

The likelihood ratio is the universally most powerful metric for discriminating between two hypotheses, according to the Neyman-Pearson lemma [20]. In our likelihood ratio test, the null hypothesis assumes that the two histograms in the comparison, each with k bins, are sampled from the joint Poisson distribution

$$P(u,v) = \prod_{i=1}^{k} \frac{\mu_i^{u_i}}{u_i!} e^{-\mu_i} \frac{\nu_i^{v_i}}{v_i!} e^{-\nu_i}, \tag{3.3.1}$$

where ν_i and μ_i are the mean bin contents (or Poisson rate) for bin i for histograms v and u respectively. The probability of getting the shape of histogram v can be modeled as the multinomial below, with our two options being that a bin value came from histogram u or v,

$$P(v|u+v=t) = \prod_{i=1}^{k} \binom{t_i}{v_i} \left(\frac{\nu_i}{\nu_i+\mu_i}\right)^{v_i} \left(\frac{\mu_i}{\nu_i+\mu_i}\right)^{t_i-v_i}. \tag{3.3.2}$$

Here, $t_i = u_i + v_i$ is fixed to be the observed total bin content.

To model our null hypothesis, we choose $\nu_i = a\mu_i$ for $i = 1,2,\ldots,k$. The value of a is taken to be the value of the maximum likelihood estimator (MLE), $\hat{a} = \frac{N_v}{N_u}$, where N_v and N_u are the integrals of histograms v and u. This assumption ensures that, even if the individual contents of the histogram bins differ, their overall shapes will be the same. For our alternative hypothesis, our MLE is $\hat{a}_i = \frac{v_i}{u_i}$, which allows for each bin to have a different scaling factor, giving rise to different shapes. The null hypothesis asserts that the histograms differ only by a constant normalization factor, but otherwise have the same shape, while for the alternative hypothesis, this normalization factor can differ bin by bin to create different shapes.

The comparison between our two hypotheses can be expressed as

$$\lambda = \frac{\max_{H_0} \mathscr{L}(a|v)}{\max_{H_1} \mathscr{L}(a_i|v)} = \prod_{i=1}^{k} \frac{\left(\frac{\hat{a}}{1+\hat{a}}\right)^{v_i} \left(\frac{1}{a+\hat{a}}\right)^{t_i-v_i}}{\left(\frac{\hat{a}_i}{1+\hat{a}_i}\right)^{v_i} \left(\frac{1}{a+\hat{a}_i}\right)^{t_i-v_i}} \tag{3.3.3}$$

Here, the likelihood is derived from our multinomial probability and is a function of our estimators, a and a_i, which are set to the MLEs of their respective hypotheses. The likelihood ratio, our test statistic, is compared to a chi-squared distribution, which is how it should behave asymptotically. From this distribution, we can obtain a p-value, which can be interpreted as the probability of obtaining this value of the likelihood ratio (or larger) under the null hypothesis. If this p-value is very small, we can assume that it is unlikely to obtain this value under H_0, and we can reject

the null hypothesis (that the shapes are similar). If this p-value is large, we fail to reject the null hypothesis and can conclude that the shapes are sufficiently similar.

We can use this p-value as a quantitative measure of similarity when making different shape comparisons for potential consolidations. In Figure 3.2 both measures of shape similarity are presented, with the direct ratio in the top plot and the results of the likelihood ratio in the bottom plot. Here, instead of presenting p-values for the individual bins, the results are displayed in terms of the number of standard deviations, σ, from the central value of the chi-squared distribution. To calculate σ, the square root of the likelihood is used to calculate the tail integral of the chi-squared distribution. The p-value on the right of the bottom plot is for the likelihood of all bins.

In the direct ratio, deviations from 1 in the top plot are deviations in shape from the consolidated histogram for a particular bin. For the likelihood ratio, a large σ value indicates a larger deviation from the central value of the test statistic, translating to larger deviations in shape. These two metrics are in good agreement, with bins that have larger discrepancies in the direct ratio also having relatively large σ values.

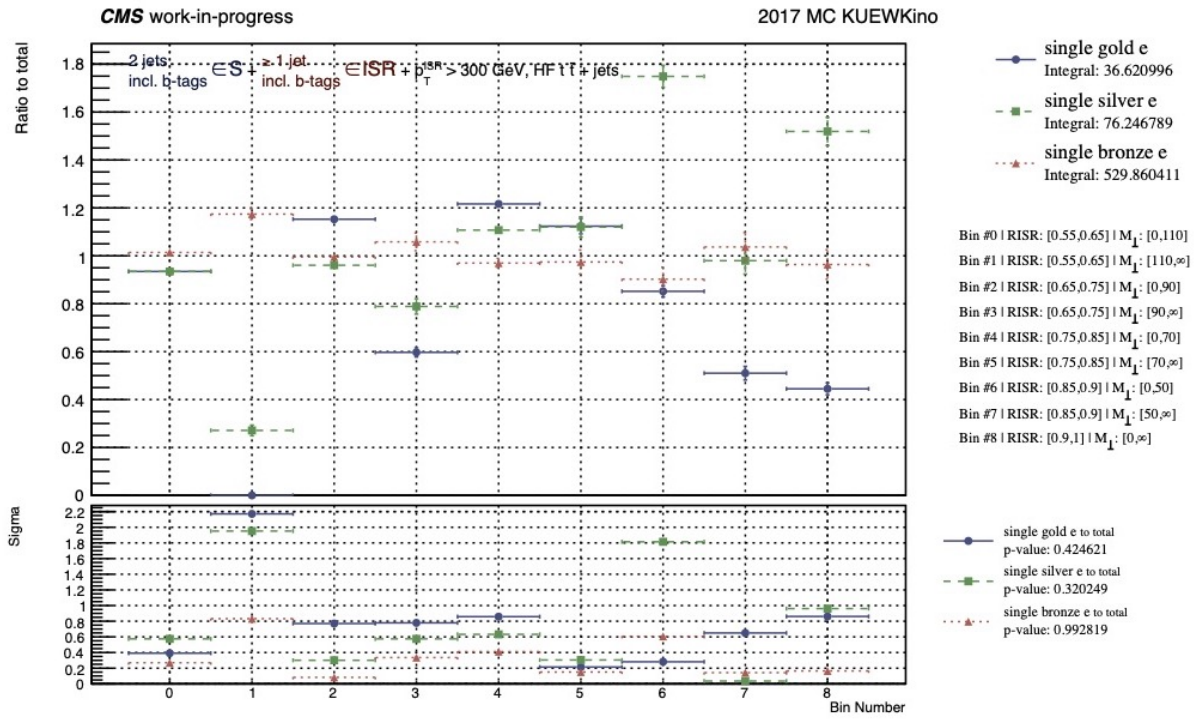

Figure 3.2: Example of a shape comparison between lepton IDs for heavy-flavor $t\bar{t}$ decays in the one lepton channel with 2 jets in the sparticle system and at least 1 jet in the ISR system.

According to these shape similarity studies, it is reasonable to combine the events with a light-flavor fake with those that have an unmatched fake. The shapes between these sources agree more than the light-flavor and heavy-flavor fake shapes, and this combination boosts the statistics of the light-flavor fake events. Shapes are further combined according to background process and other categories listed in Table 2.4. These shape combinations drive the groups of categories whose fake lepton shape variations are connected with a common nuisance parameter. The combinations also inform histogram consolidations, which forms the basis of our smoothing procedure, outlined in Section 3.3.2

3.3.2 Histogram smoothing procedure

Separate from our fake treatment, we employ a smoothing procedure to create consolidated histograms, summing over analysis categories that should behave similarly, as determined by the procedure in Section 3.3.1, to serve as the central value on which to impose simulated variations. The goal for this method is to create a more robust and computationally tractable fit by replacing low statistic bins with statistically consistent yields. Some histogram bins may have few or no simulated events. However, this may not be the case in data. To more accurately reflect the statistics in data, we can systematically replace bins in the original simulated histogram for bins with higher event counts from the consolidated template.

We create consolidated histograms, summing over histograms in analysis categories that should behave similarly in terms of shape for fake lepton events. The comparison studies outlined in Section 3.3.1 determined which categories to combine. Other categories are consolidated due to limited statistics. For example, our consolidated shapes and systematic variations are separated according to fake source (how the fake originated in the event). The two physical sources of fakes that we consider are the decays of heavy-flavor quarks and light-flavor quarks. In Monte Carlo simulation, a fake may also arise from an “unmatched" reconstructed lepton, that is, a reconstructed lepton that could not be matched to a true, generator-level lepton. For example, in the CMS detector, these kinds of leptons may result from hadronic jet punch-throughs into the muon chambers,.

In our simulated samples, the number of events with light-flavor fakes is low relative to the two other sources of fake leptons.

Shape templates are separated by the decay channel, and for events with more than one lepton, the shapes are combined over the combinatoric assignment in the sparticle system. In other words, the shape for events with two leptons in the *a* hemisphere is combined with that of two leptons in the *b* hemisphere, and with that of one lepton in either hemisphere. This consolidation procedure connects the variations of categories that should behave similarly in terms of variations due to fake leptons. This method will also fill in empty bins due to limited Monte Carlo statistics. We create separate, central value histograms for different lepton IDs, lepton flavors, and fake sources. All other analysis categories listed in Table 2.4 are summed over.

Once we have adequately combined analysis categories for consolidated histograms, we can use these newly formed templates to fill in gaps in the original histograms. The replacement procedure is as follows: An individual histogram h with n bins is first unweighted (such that we are only dealing with the effective event counts that follow a Poisson distribution) and normalized to unity. Then, we iterate through each unweighted, normalized bin b and compare this value to a minimum required bin count. For this analysis, that minimum value is 10 events to potentially avoid the computationally expensive method of modeling per-process uncertainties. The method used to compute statistical uncertainties is called the Barlow-Beeston-lite method [21] and it is used in the statistical analysis package HiggsCombine. Using this method the uncertainties are modeled by a single Gaussian for all processes that contribute to bin b for bins in this “high-event" regime (defaulting to at least 10 events/bin). Bins with effective event counts below this threshold cannot have their per-process uncertainties approximated by Gaussians, so they are separately parameterized by Poisson distributions. If bin b falls below this threshold of minimum event count, its replaced value is the minimum of the remaining normalized integral and the value for the consolidated histogram at bin b, renormalized to the remaining integral of the individual histogram. Assigning new bin values in this manner maintains shape consistency and provides plausible new event counts. This replacement scheme will provide better results for fitting the likelihood model

to data, due to increased statistics.

We can check the agreement between the shapes of the individual histogram and its recreated version using the likelihood ratio test in the same manner described above. We can set the errors in the recreated histograms to systematically cover any extreme changes in bin values. With these recreated histograms, we impose variations in our discriminating variables to simulate shape changes due to fake leptonic backgrounds, as described in Section 3.3.

Control Region Fit Results

The aim of our shape-based fake estimation method is to give our fit to data degrees of freedom it otherwise wouldn't have. By allowing the shape to change (within some given 1σ variation, seen in Figure 3.1), the fit can better discern between changes in shape due to fake lepton mis-modeling or an alternative hypothesis (i.e. signal). In Section 3.3, we described the general procedure for our shape-based fake estimation method, which currently includes a maximum deviation of 5% from the nominal value. To evaluate the effectiveness of this method, we can look at the differences in the pre- and post-fit results for the central values and errors on the parameters. We expect the pre-fit value of the NP (θ_{pre}) to be similar to its post-fit value (θ_{post}), quantified by the pull of this parameter,

$$\frac{\theta_{\text{post}} - \theta_{\text{pre}}}{\sigma_{\text{pre}}} = \frac{\Delta x}{\sigma_{\text{in}}} \,, \tag{4.0.1}$$

where σ_{pre} is the pre-fit uncertainty. The uncertainty on this value should become "constrained" or "profiled," meaning that the fit was able to provide a smaller uncertainty than the pre-fit value. This profiling can be quantified by looking at the ratio of pre- to post-fit uncertainties,

$$\sigma_{\text{post}}/\sigma_{\text{pre}} = \sigma_{\text{out}}/\sigma_{\text{in}} \,, \tag{4.0.2}$$

which should be less than 1 if this NP was able to be constrained. If this value is equal to 1, this means that the fit was not able to provide any more information about this NP than what we gave it.

As for the overall sensitivity of the analysis, we can calculate exclusion limits to predict where points for a grid of mass splittings ($m_{\tilde{P}}$ vs. $\Delta M = m_{\tilde{P}} - m_{\tilde{\chi}_1^0}$) would be excluded by a 95% confidence level. We would like the excluded parent masses, $m_{\tilde{P}}$, to be as high as possible in order to set stringent limits. Because this analysis is specifically designed to target compressed scenarios, we also expect to be able to exclude very small mass splittings between the parent and child mass, ΔM. Ideally, this fake estimation method would not significantly degrade these exclusion limits, potentially improving them. For the scope of this paper, we are interpreting results in the framework of electroweakino pair production, or the TChiWZ model (Figure 1.3), such that $m_{\tilde{P}} = \mathrm{m}_{\tilde{\chi}_1^\pm}$ is the chargino mass and $m_{\tilde{\chi}_1^0}$ is the LSP mass.

Because the analysis has not yet been approved to unblind our data, to reduce bias the results including data presented here are for control regions (CRs). This means that regions where we expect to see the most signal events are not included. These signal regions in particular are the high R_{ISR} bins (typically [0.85,1]) and the corresponding $M_\perp$ values. To further reduce our signal bias, these fits shown are for the background-only (null) hypothesis, which means that the signal cross-section is fixed to zero.

As such, these results are not as sensitive to any of our signals as we fully expect them to be, but can still give us a good estimate of how effective the fake lepton estimation method is. There are also more systematics (such as jet energy scale corrections and PDF normalizations) that still need to be added to the fit.

The fake lepton shape systematics are the parameters that follow a naming convention of

$$[leptonFlavor][fakeSource]\_\mathrm{Fake}\_[\#leptons]\_[\#sJets]\_[type] \tag{4.0.3}$$

A fake source of 0 indicates a light-flavor or unmatched fake lepton while a fake source of 1 is a fake lepton originating from a heavy-flavor decay. "Type" refers to whether this systematic is due to an R_{ISR} or $M_\perp$ variation. From the naming convention above, one can see that these shape nuisance parameters are connected across background processes and analysis categories including

lepton quality, ISR jet multiplicity, and b-tag counting in the sparticle system.

b-only fit	
name	$\Delta x/\sigma_{\text{in}}$, $\sigma_{\text{out}}/\sigma_{\text{in}}$
muf0_Fake_3L_inclJS_RISR	-0.04, 1.00
muf0_Fake_3L_0J_RISR	+0.39, 0.95
muf0_Fake_2L_2J_RISR	+1.13, 0.77
muf0_Fake_2L_2J_Mperp	-2.10, 0.80
muf0_Fake_2L_1J_RISR	+0.35, 0.81
muf0_Fake_2L_1J_Mperp	-0.57, 0.88
muf0_Fake_2L_0J_RISR	-0.01, 0.88
muf0_Fake_2L_0J_Mperp	+0.58, 0.90
muf0_Fake_1L_ge4J_RISR	+0.18, 0.97
muf0_Fake_1L_ge4J_Mperp	-0.22, 0.97
muf0_Fake_1L_3J_RISR	+0.17, 0.97
muf0_Fake_1L_3J_Mperp	-0.07, 0.98
muf0_Fake_1L_2J_RISR	+0.51, 0.98
muf0_Fake_1L_2J_Mperp	+0.26, 0.97
muf0_Fake_1L_1J_RISR	-0.03, 0.98
muf0_Fake_1L_1J_Mperp	-0.03, 0.99
muf0_Fake_1L_0J_RISR	+0.07, 0.99
muf0_Fake_1L_0J_Mperp	-0.21, 0.99

Table 4.1: Pulls for heavy flavor fake muon shape nuisance parameters for fit to 2016 data.

Background-only fits were done across all lepton channels for individual years to the designated control regions of the Run II dataset. Tables 4.1, 4.2, and 4.3 show the pulls for background-only fits to control regions for all lepton channels and categorizations for, respectively 2016, 2017, and 2018 Run II data with a compressed electroweakino pair production scenario ($m_{\tilde{\chi}_1^\pm} = 400$ GeV, $m_{\tilde{\chi}_1^0} = 390$ GeV). This signal point was produced from the inclusive TChiWZ sample for each year, which only covers mass splittings up to 50 GeV [1]. These tables show the pulls for the fake lepton shape systematics corresponding to at least one heavy flavor fake muon. Pulls for the rest of the nuisance parameters in the fits can be found in the tables in Appendix A. It should be noted that the systematic configuration is slightly different in 2016 than the ones in 2017 and 2018. Because we expect to have fewer issues with W + jets mis-modeling for 2016, the W + jets normalizations

[1] 2016 sample: `TChiWZ_genHT-160_genMET-80_TuneCUETP8M1_13TeV-madgraphMLM-pythia8_Summer16_102X.root`, 2017 sample: `TChiWZ_genHT-160_genMET-80_TuneCP2_13TeV-madgraphMLM-pythia8_Fall17_102X.root`, 2018 sample: `TChiWZ_genHT-160_genMET-80_TuneCP2_13TeV-madgraphMLM-pythia8_Autumn18_102X.root`

for different sparticle jet regions are included with the other backgrounds in the “norm_bkgs" factors. This set of normalizations (“norm_Wjets") is separate from “norm_bkgs" for 2017 and 2018 fits.

b-only fit	
name	$\Delta x/\sigma_{\text{in}}$, $\sigma_{\text{out}}/\sigma_{\text{in}}$
muf0_Fake_3L_inclJS_RISR	+0.05, 1.00
muf0_Fake_3L_0J_RISR	+0.46, 0.95
muf0_Fake_2L_2J_RISR	+0.70, 0.70
muf0_Fake_2L_2J_Mperp	+0.73, 0.69
muf0_Fake_2L_1J_RISR	+0.05, 0.74
muf0_Fake_2L_1J_Mperp	+0.86, 0.79
muf0_Fake_2L_0J_RISR	+1.27, 0.83
muf0_Fake_2L_0J_Mperp	+0.17, 0.89
muf0_Fake_1L_ge4J_RISR	-1.09, 0.97
muf0_Fake_1L_ge4J_Mperp	-0.99, 0.98
muf0_Fake_1L_3J_RISR	-0.17, 0.95
muf0_Fake_1L_3J_Mperp	+0.12, 0.95
muf0_Fake_1L_2J_RISR	-0.08, 0.97
muf0_Fake_1L_2J_Mperp	+0.28, 0.96
muf0_Fake_1L_1J_RISR	-0.07, 0.98
muf0_Fake_1L_1J_Mperp	-0.11, 0.97
muf0_Fake_1L_0J_RISR	-0.34, 0.99
muf0_Fake_1L_0J_Mperp	+0.32, 0.99

Table 4.2: Pulls for heavy flavor fake muon shape nuisance parameters for fit to 2017 data.

Most of the fake lepton shape systematics have pulls ($\Delta x/\sigma_{\text{in}}$) near zero, which means that the central value shape moves around slightly within the given $\pm 1\sigma$ variation, but not significantly. For these fits, the given $\pm 1\sigma$ variation, or *a priori* uncertainty, for the fake lepton shape systematics is 5%. Without these important systematics, these slight variations in shape could be incorrectly attributed to signal processes affect the shape of our distribution. However, there are certain systematics whose pulls vary significantly from zero. For example, in 2018, the parameter `muf0_Fake_1L_0J_Mperp` has a pull of -2.41, which means that the value of the parameter after the fit decreased by about 10%. This change can be interpreted as a 10% change in shape for the heavy flavor fake muon $M_{\perp}$ distributions that have a reconstructed lepton and no jets in the sparticle system. It is promising that a change in shape like this can be captured by these particular

parameters, instead of being incorrectly attributed to the presence of a potential signal.

b-only fit	
name	$\Delta x/\sigma_{\text{in}}$, $\sigma_{\text{out}}/\sigma_{\text{in}}$
muf0_Fake_3L_inclJS_RISR	-0.04, 0.99
muf0_Fake_3L_0J_RISR	-0.11, 0.90
muf0_Fake_2L_2J_RISR	-0.23, 0.49
muf0_Fake_2L_2J_Mperp	+0.10, 0.48
muf0_Fake_2L_1J_RISR	+0.61, 0.55
muf0_Fake_2L_1J_Mperp	-0.38, 0.66
muf0_Fake_2L_0J_RISR	+0.08, 0.65
muf0_Fake_2L_0J_Mperp	-1.30, 0.75
muf0_Fake_1L_ge4J_RISR	-2.37, 0.85
muf0_Fake_1L_ge4J_Mperp	-1.90, 0.90
muf0_Fake_1L_3J_RISR	+0.68, 0.87
muf0_Fake_1L_3J_Mperp	-0.40, 0.89
muf0_Fake_1L_2J_RISR	+1.27, 0.90
muf0_Fake_1L_2J_Mperp	+0.68, 0.87
muf0_Fake_1L_1J_RISR	+1.15, 0.94
muf0_Fake_1L_1J_Mperp	+0.42, 0.93
muf0_Fake_1L_0J_RISR	+1.14, 0.96
muf0_Fake_1L_0J_Mperp	-2.41, 0.98

Table 4.3: Pulls for heavy flavor fake muon shape nuisance parameters for fit to 2018 data.

These shape NPs also have error bars ($\sigma_{\text{out}}/\sigma_{\text{in}}$) of width approximately one, which means that the prior $\pm 1\sigma$ variation also does not change compared to the post-fit value. The smaller error bars indicate that the fit was able to evaluate the size of these shape variations more precisely than the *a priori* uncertainty. It is good that these post-fit uncertainties are slightly smaller than we originally gave the fit so we can more precisely capture the effect of these parameters. However, none of the fake shape systematics are overly constrained–with error bars much less than 1. This indicates that even with all of the extra degrees of freedom, or variance, that we gave the model, it is not overfitting to the data.

In terms of other systematics, the fits shown here also included floating scale factors as a data-driven method for measuring the cross-sections of more dominant SM backgrounds (like $\text{W}+\text{jets}$ and $\text{t}\bar{\text{t}}$). These NPs do not show up in the tables because there is no prior uncertainty on them, so there is no θ_{pre} to calculate Δx. The tables in Appendix A show the pulls for the other nuisance

parameters, including systematics that account for the W + jets mis-modelling effects in 2017 and 2018. These W + jets specific parameters are separated by lepton and sparticle jet multiplicities to account for this mis-modelling that increases with jet count. As such, we expect an increase in the pulls in these W + jets systematics as the sparticle jet count increases. While the shape systematics for the fake lepton estimation method are finalized in the fit, other systematics in the fit are still under development. Specifically for W + jets, any particularly high pulls in these control regions fits will be studied in further detail.

Another way to evaluate the effectiveness of the additional fake lepton shape parameters is to analyze how the shape of the R_{ISR}-$M_{\perp}$ distribution changes before and after the fit was performed. As stated in Section 3, the reason we introduce these additional shape parameters into the fit is to capture mismodeling effects from fake leptons that could affect the shape of the R_{ISR}-$M_{\perp}$ distribution. So, if the fit uses these degrees of freedom to adjust the background model to better describe our data, we can conclude that these parameters were a successful addition to the fit. Examples of these pre- and post-fit R_{ISR}-$M_{\perp}$ distributions can be seen in Figures 4.1, 4.2, and 4.3 for 2016, 2017, and 2018 data respectively. The top plot in both of these figures is the distribution before (pre) the fit and the one on bottom is the distribution after (post) the fit. In this case, like the fits for the pull tables, this fit is a background-only fit, meaning that the value of the signal strength is fixed to zero.

Since the yields between data and Monte Carlo are both fairly high, it is difficult to see the discrepancies in the absolute number of events. However, the ratio between data and the background model (below the histogram) clarifies these discrepancies, and the trends in these discrepancies among the R_{ISR}-$M_{\perp}$ bins. From these ratio plots, we can see that any trends in the discrepancies (i.e. increasing or decreasing) across the R_{ISR} or $M_{\perp}$ bins are flattened out due to the addition of these shape parameters, since they allow the distribution to move bin-by-bin rather than cohesively It also is apparent that the fit is able to adjust the parameter values to better describe our data in these control regions, since across the distribution, the ratio of data to MC becomes closer to 1 in each bin. The errors, represented by the shade regions in each bin, are also profiled down. This

effect echos what was observed in the fake lepton shape parameter pulls, where the errors on these NPs become smaller after the fit, meaning that the fit was able to more provide a more precise value for the systematics compared to what it was initially given.

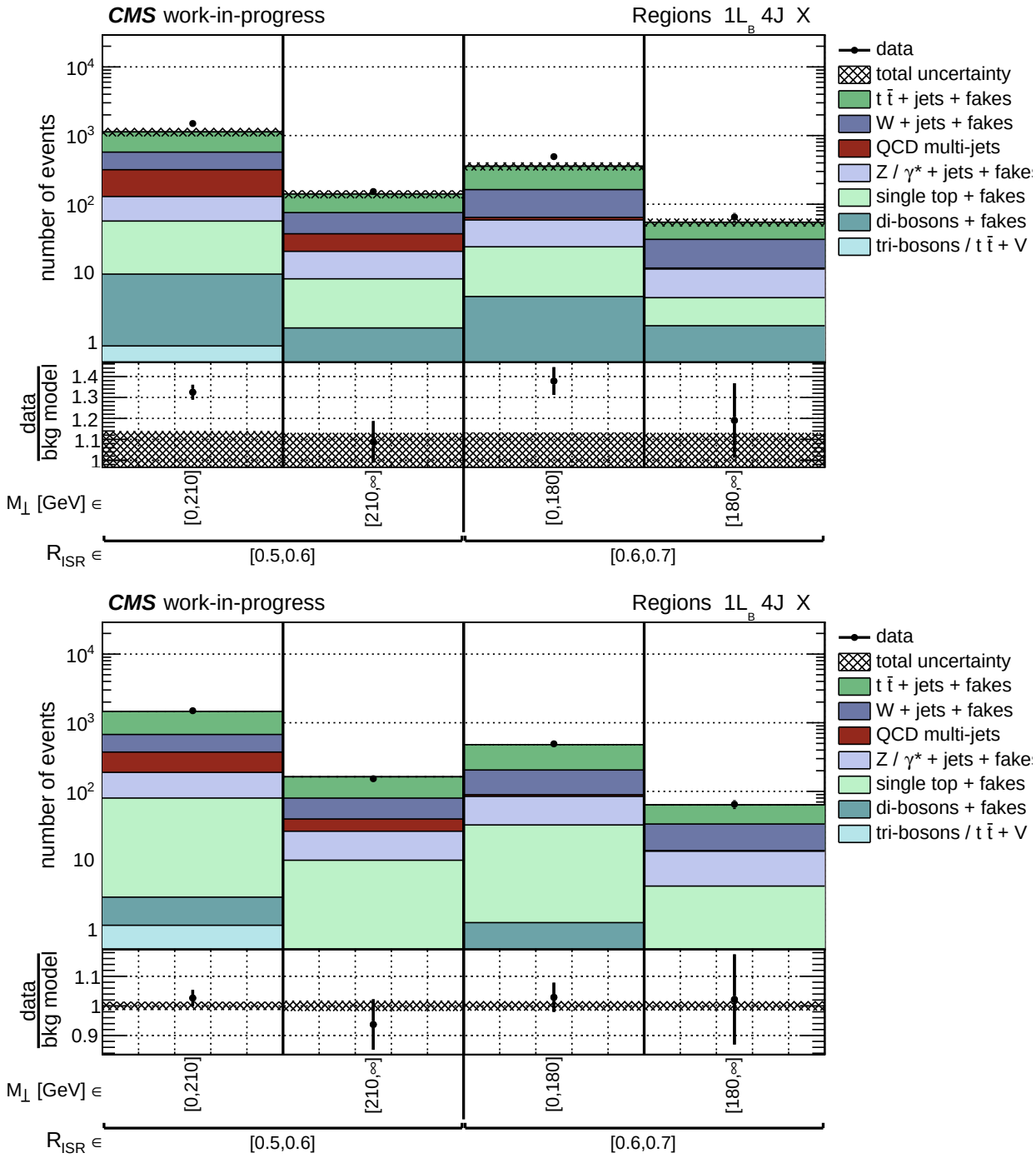

Figure 4.1: R_{ISR} and $M_{\perp}$ pre- and post-fit distributions. Top: Pre-fit to the 1 bronze lepton 4 S jet control region in 2016. Bottom: Background only fit to the 1 bronze lepton 4 S jet control region in 2016.

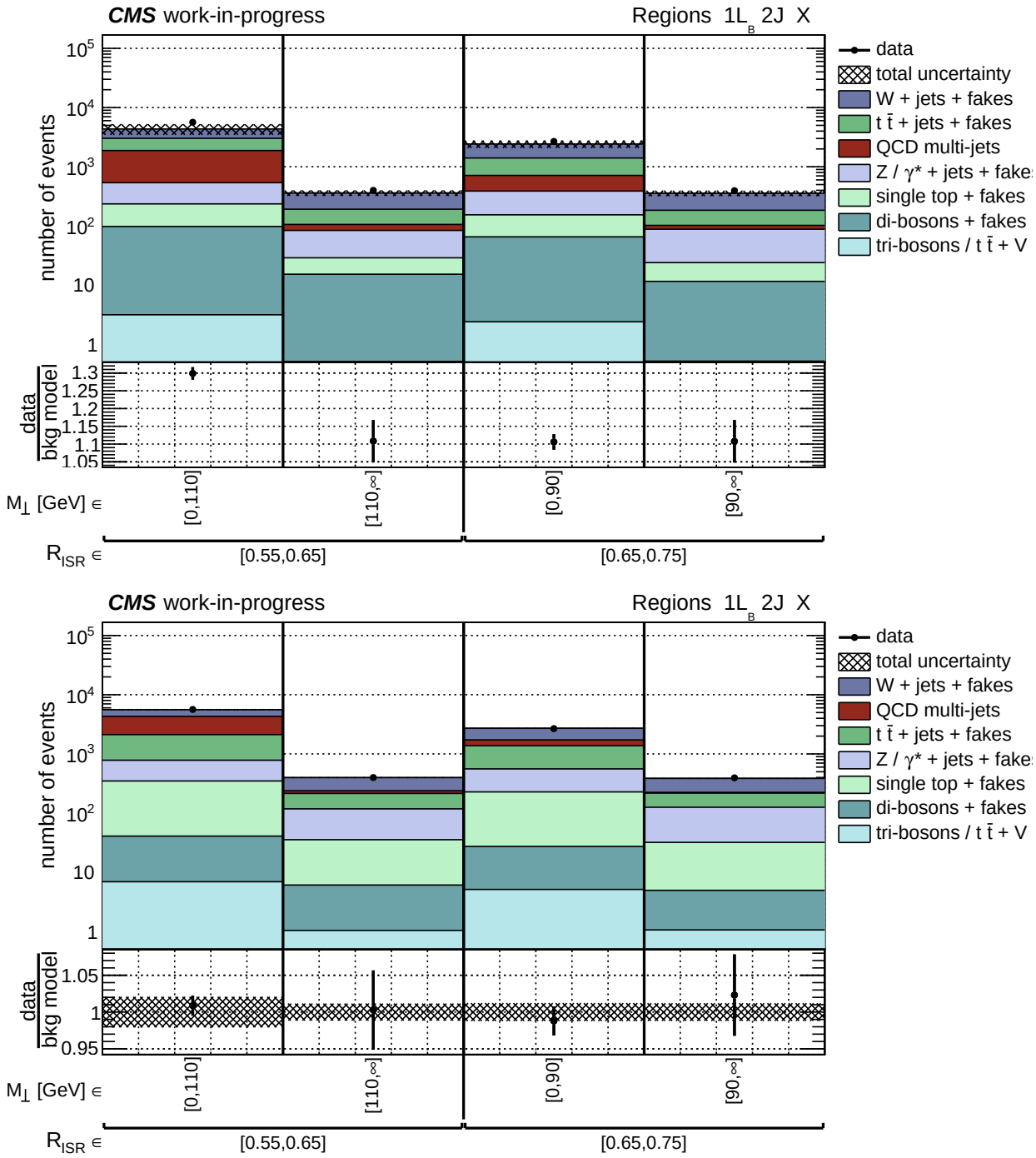

Figure 4.2: R_{ISR} and $M_{\perp}$ pre- and post-fit distributions. Top: Pre-fit to the 1 bronze leptons 2 S jet control region in 2017. Bottom: Background only fit to the 1 bronze leptons 2 S jet control region in 2017.

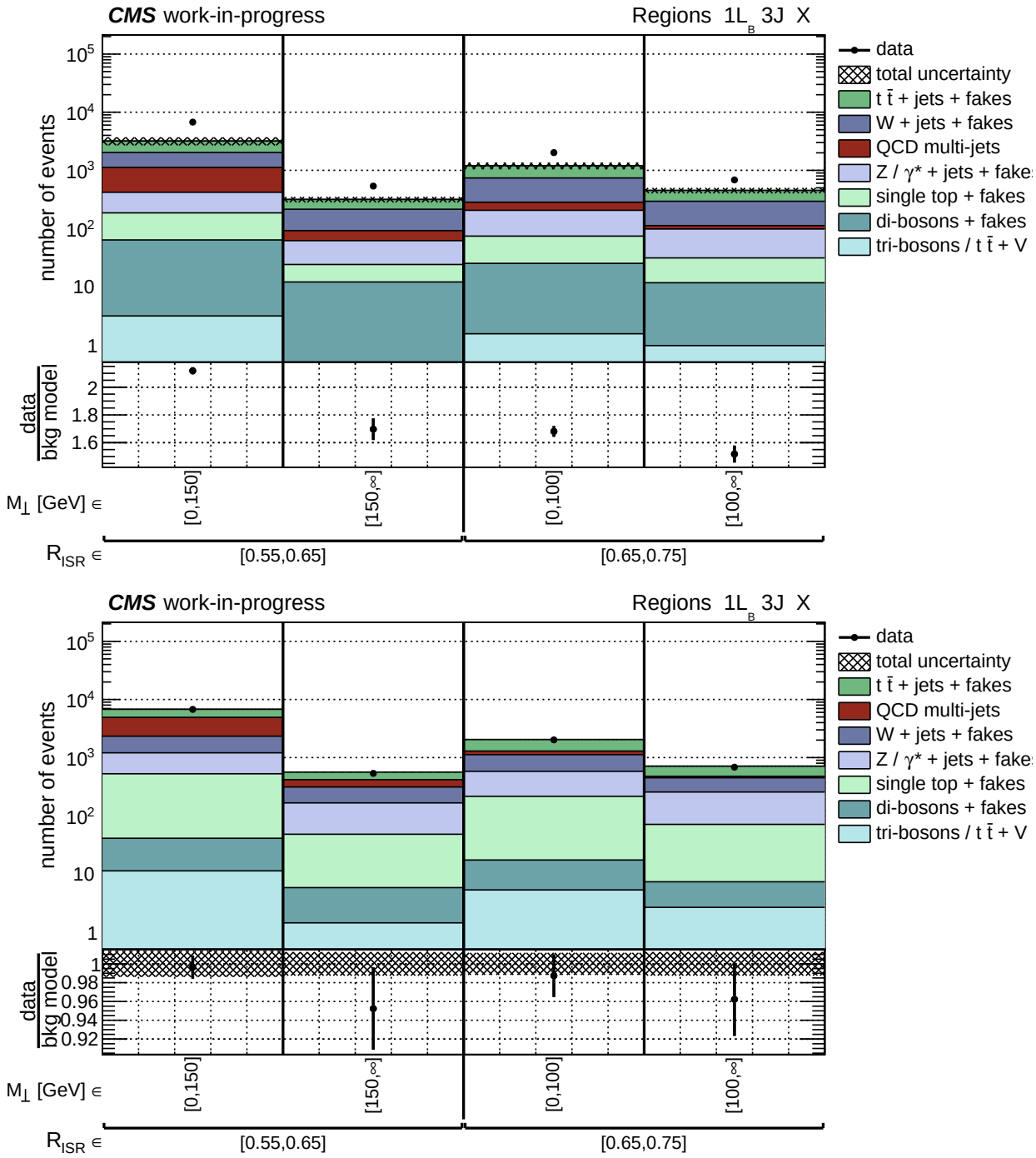

Figure 4.3: R_{ISR} and $M_{\perp}$ pre- and post-fit distributions.Top: Pre-fit to the 1 bronze leptons 3 S jet control region in 2018. Bottom: Background only fit to the 1 bronze leptons 3 S jet control region in 2018.

Expected Sensitivity

Now that we are confident that the addition of the fake shape parameters did not negatively affect or over-constrain the fit, we can calculate exclusion limits for the TChiWZ grid. Here we focus on the extremely compressed regime with only inclusive TChiWZ samples. Figure 5.1 shows the expected exclusion limits for 2017 Monte Carlo, scaled up to 137.2 fb^{-1}. This plot shows the limits in the 2D plane of the mass difference between the chargino and LSP, and the LSP mass. The color axis corresponds to the cross section at that area of phase space at 95% confidence level. The limits in Figure 5.1 were produced by fits to only simulated MC events with the signal regions included. This plot focuses on the limits in the compressed region of this signal grid and were produced with the same inclusive TChiWZ sample as the fits in Section 4.

This analysis was designed to target highly compressed scenarios and we can begin to see this pay off in Figure 5.1. These expected limits show a slight increase in sensitivity at lower mass splittings, even for high parent sparticle masses, compared to current limits. The limits in the compressed region are largely independent of the LSP mass, demonstrated by a mostly vertical line in the compressed region plot. This indicates that our sensitivity in compressed regions is not dependent on this parameter.

The fits for the limits shown here are the same as those in Section 4, just over multiple mass points for the TChiWZ signal. These preliminary limits could potentially set the most stringent limits on this particular signal for CMS. We expect our analysis to also have sensitivity other signal processes, especially in this compressed regime. Current limits for the pair production of a

chargino-neutralino pair for CMS only extend up to a chargino mass of below 280 GeV at a mass difference of 10-20 GeV [22, 23, 24]. Our preliminary expected limits show our analysis to be sensitive to a chargino with a mass of 350 GeV at a very compressed mass splitting of 10 GeV, far surpassing current exclusion limits.

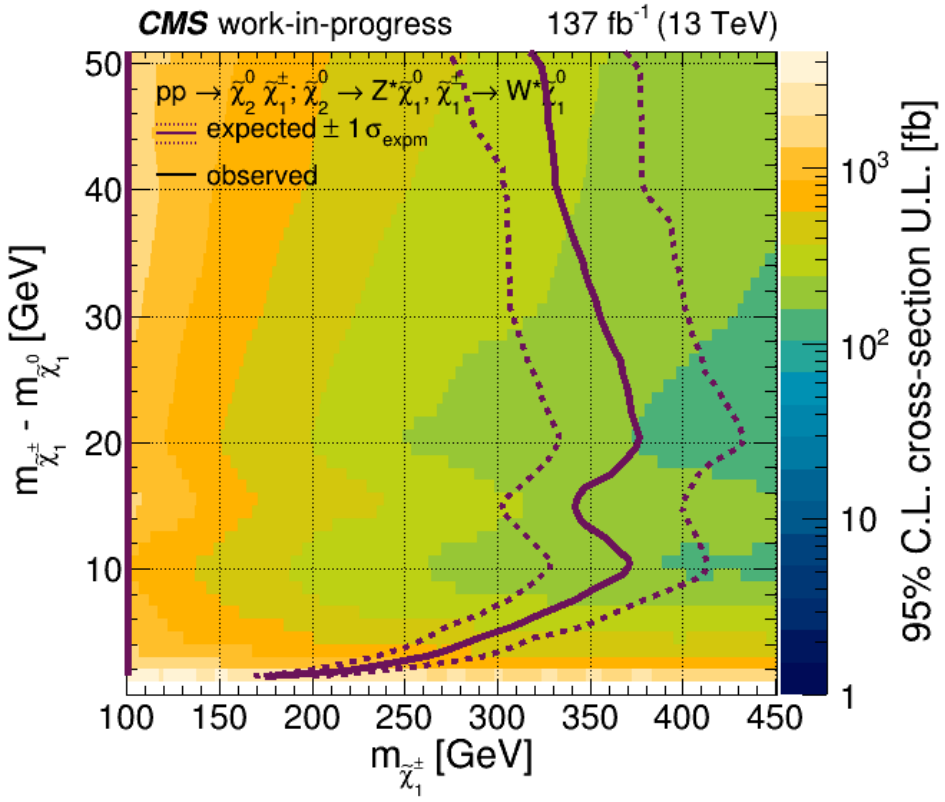

Figure 5.1: Expected limits for TChiWZ cross-section at 95% CL. The limits are computed using the TChiWZ and background MC from 2017 scaled to 137.2 fb^{-1} and include the signal sensitive regions.

Conclusion

While the Standard Model may still pose unanswered questions, the theory of SUSY aims to complete this picture in a relatively simple and intuitive manner by extending the symmetry already present in the SM. Experimentalists at colliders, such as the LHC, are currently searching for evidence of SUSY with detectors like the CMS detector. The analysis presented here searches for SUSY using the Recursive Jigsaw Reconstruction method and features a new, shape-based method of estimating the background contribution due to fake leptons. This shape-based method allows for a more general fit than is typically used that can account for variations in the data which could otherwise be potentially interpreted as signal. The extra systematics do not over-constrain our fit to data, but rather, provide it with extra degrees of freedom to fit the background more precisely than the traditional fake-to-loose method. While this analysis is still in progress, preliminary results demonstrate the potential to probe smaller mass splittings with higher parent sparticle masses than previously explored at the LHC.

References

[1] P. Zyla *et al.*, "Review of Particle Physics", *PTEP*, vol. 2020, no. 8, p. 083C01, 2020. DOI: 10.1093/ptep/ptaa104.

[2] J. Woithe, J. Wiener, and F. Van der Veken, "Let's have a coffee with the standard model of particle physics!", *Physics Education*, vol. 52, pp. 34 001–34 010, Mar. 2017. DOI: 10.1088/1361-6552/aa5b25.

[3] A. Collaboration, "Observation of a new particle in the search for the standard model higgs boson with the atlas detector at the lhc", *Physics Letters B*, vol. 716, no. 1, pp. 1–29, Sep. 2012, ISSN: 0370-2693. DOI: 10.1016/j.physletb.2012.08.020. [Online]. Available: http://dx.doi.org/10.1016/j.physletb.2012.08.020.

[4] C. Collaboration, "Observation of a new boson at a mass of 125 gev with the cms experiment at the lhc", *Physics Letters B*, vol. 716, no. 1, pp. 30–61, Sep. 2012, ISSN: 0370-2693. DOI: 10.1016/j.physletb.2012.08.021. [Online]. Available: http://dx.doi.org/10.1016/j.physletb.2012.08.021.

[5] S. P. Martin, "A supersymmetry primer", *Advanced Series on Directions in High Energy Physics*, pp. 1–98, Jul. 1998, ISSN: 1793-1339. DOI: 10.1142/9789812839657_0001. [Online]. Available: http://dx.doi.org/10.1142/9789812839657_0001.

[6] O. Brüning, *LHC design report Vol. 1. Vol. 1*. 2004, OCLC: 723186985, ISBN: 978-92-9083-224-9.

[7] C. Collaboration, *CMS Physics: Technical Design Report Volume 1: Detector Performance and Software*, ser. Technical design report. CMS. Geneva: CERN, 2006, There is an error on cover due to a technical problem for some items. [Online]. Available: https://cds.cern.ch/record/922757.

[8] P. Jackson and C. Rogan, "Recursive jigsaw reconstruction: Hep event analysis in the presence of kinematic and combinatoric ambiguities", *Physical Review D*, vol. 96, no. 11, Dec. 2017, ISSN: 2470-0029. DOI: 10.1103/physrevd.96.112007. [Online]. Available: http://dx.doi.org/10.1103/PhysRevD.96.112007.

[9] P. Jackson, C. Rogan, and M. Santoni, "Sparticles in motion: Analyzing compressed susy scenarios with a new method of event reconstruction", *Physical Review D*, vol. 95, no. 3, Feb. 2017, ISSN: 2470-0029. DOI: 10.1103/physrevd.95.035031. [Online]. Available: http://dx.doi.org/10.1103/PhysRevD.95.035031.

[10] N. Polonsky, "Supersymmetry Structure and Phenomena", *arXiv:hep-ph/0108236*, Aug. 2001, arXiv: hep-ph/0108236. [Online]. Available: http://arxiv.org/abs/hep-ph/0108236 (visited on 05/10/2021).

[11] *The CMS hadron calorimeter project: Technical Design Report*, ser. Technical design report. CMS. Geneva: CERN, 1997, The following files are from here and may not be the version as printed, please check the printed version to be sure. [Online]. Available: https://cds.cern.ch/record/357153.

[12] J. G. Layter, *The CMS muon project: Technical Design Report*, ser. Technical design report. CMS. Geneva: CERN, 1997. [Online]. Available: https://cds.cern.ch/record/343814.

[13] CMS E/gamma Physics Object Group. (Jun. 6, 2020). Cut based electron ID for run 2, [Online]. Available: https://twiki.cern.ch/twiki/bin/view/CMS/CutBasedElectronIdentificatio Electron_ID_Working_Points_WP_de (visited on 07/08/2021).

[14] CMS Muon Physics Object Group. (Nov. 28, 2019). Baseline muon selections for run-II, [Online]. Available: https://twiki.cern.ch/twiki/bin/viewauth/CMS/SWGuideMuonIdRun2#Medium_Muon (visited on 07/08/2021).

[15] C. Collaboration, "Identification of heavy-flavour jets with the CMS detector in pp collisions at 13 TeV", *Journal of Instrumentation*, vol. 13, no. 5, P05011–P05011, May 8, 2018, ISSN: 1748-0221. DOI: 10.1088/1748-0221/13/05/P05011. [Online]. Available: https://iopscience.iop.org/article/10.1088/1748-0221/13/05/P05011 (visited on 05/18/2021).

[16] E. Schmitz, "Search for production of supersymmetric top quarks in hadronic and multi-leptonic final states, using a deep neural network based soft b-tagger for compressed mass scenarios", PhD thesis, The University of Kansas, 2021.

[17] J. S. Conway, *Incorporating nuisance parameters in likelihoods for multisource spectra*, 2011. DOI: 10.48550/ARXIV.1103.0354. [Online]. Available: https://arxiv.org/abs/1103.0354.

[18] F. Porter, *Goodness-of-fit – considerations and comparisons; example: Testing consistency of two histograms*, Feb. 2008. [Online]. Available: http://www.hep.caltech.edu/~fcp/statistics/lectures0802/L0802C.pdf.

[19] ——, *Goodness-of-fit: Considerations and comparisons*, Feb. 2008. [Online]. Available: http://www.hep.caltech.edu/~fcp/statistics/lectures0802/L0802C.pdf.

[20] J. Neyman, E. S. Pearson, and K. Pearson, "IX. on the problem of the most efficient tests of statistical hypotheses", *Philosophical Transactions of the Royal Society of London. Series A, Containing Papers of a Mathematical or Physical Character*, vol. 231, no. 694, pp. 289–337, Feb. 16, 1933, Publisher: Royal Society. DOI: 10.1098/rsta.1933.0009. [Online]. Available: https://royalsocietypublishing.org/doi/10.1098/rsta.1933.0009 (visited on 03/03/2022).

[21] R. Barlow and C. Beeston, "Fitting using finite monte carlo samples", *Computer Physics Communications*, vol. 77, no. 2, pp. 219–228, 1993, ISSN: 0010-4655. DOI: https://doi.org/10.1016/0010-4655(93)90005-W. [Online]. Available: https://www.sciencedirect.com/science/article/pii/001046559390005W.

[22] C. Collaboration, "Search for supersymmetry with a compressed mass spectrum in the vector boson fusion topology with 1-lepton and 0-lepton final states in proton-proton collisions at \sqrtΓ"4266308sΓ"5267309 = 13 TeV", *Journal of High Energy Physics*, vol. 2019, no. 8, Aug. 2019. DOI: 10.1007/jhep08(2019)150. [Online]. Available: https://doi.org/10.1007%2Fjhep08%282019%29150.

[23] ——, "Search for new physics in events with two soft oppositely charged leptons and missing transverse momentum in proton–proton collisions at s=13tev", *Physics Letters B*, vol. 782, pp. 440–467, Jul. 2018. DOI: 10.1016/j.physletb.2018.05.062. [Online]. Available: https://doi.org/10.1016%2Fj.physletb.2018.05.062.

[24] ——, "Search for supersymmetry in final states with two or three soft leptons and missing transverse momentum in proton-proton collisions at $\sqrt{s}$ = 13 tev", 2021. DOI: 10.48550/ARXIV.2111.06296. [Online]. Available: https://arxiv.org/abs/2111.06296.

Pulls of Nuisance Parameters in Background-only Fits to Control Regions

A.1 2016 Pulls

b-only fit	
name	$\Delta x/\sigma_{\text{in}}$, $\sigma_{\text{out}}/\sigma_{\text{in}}$
muf0_Fake_3L_inclJS_RISR	-0.04, 1.00
muf0_Fake_3L_0J_RISR	+0.39, 0.95
muf0_Fake_2L_2J_RISR	+1.13, 0.77
muf0_Fake_2L_2J_Mperp	-2.10, 0.80
muf0_Fake_2L_1J_RISR	+0.35, 0.81
muf0_Fake_2L_1J_Mperp	-0.57, 0.88
muf0_Fake_2L_0J_RISR	-0.01, 0.88
muf0_Fake_2L_0J_Mperp	+0.58, 0.90
muf0_Fake_1L_ge4J_RISR	+0.18, 0.97
muf0_Fake_1L_ge4J_Mperp	-0.22, 0.97
muf0_Fake_1L_3J_RISR	+0.17, 0.97
muf0_Fake_1L_3J_Mperp	-0.07, 0.98
muf0_Fake_1L_2J_RISR	+0.51, 0.98
muf0_Fake_1L_2J_Mperp	+0.26, 0.97
muf0_Fake_1L_1J_RISR	-0.03, 0.98
muf0_Fake_1L_1J_Mperp	-0.03, 0.99
muf0_Fake_1L_0J_RISR	+0.07, 0.99
muf0_Fake_1L_0J_Mperp	-0.21, 0.99

Table A.1: Pulls for heavy flavor fake muon shape nuisance parameters for fit to 2016 data.

b-only fit	
name	$\Delta x/\sigma_{\text{in}}$, $\sigma_{\text{out}}/\sigma_{\text{in}}$
muf1_Fake_3L_inclJS_RISR	-0.14, 0.97
muf1_Fake_3L_0J_RISR	+0.36, 0.96
muf1_Fake_2L_2J_RISR	+0.70, 0.55
muf1_Fake_2L_2J_Mperp	-0.90, 0.56
muf1_Fake_2L_1J_RISR	+0.23, 0.55
muf1_Fake_2L_1J_Mperp	-0.38, 0.65
muf1_Fake_2L_0J_RISR	+0.17, 0.58
muf1_Fake_2L_0J_Mperp	+0.41, 0.72
muf1_Fake_1L_ge4J_RISR	-0.17, 0.85
muf1_Fake_1L_ge4J_Mperp	-0.87, 0.88
muf1_Fake_1L_3J_RISR	+0.61, 0.80
muf1_Fake_1L_3J_Mperp	-0.73, 0.87
muf1_Fake_1L_2J_RISR	+1.08, 0.77
muf1_Fake_1L_2J_Mperp	-0.67, 0.85
muf1_Fake_1L_1J_RISR	-0.39, 0.78
muf1_Fake_1L_1J_Mperp	-1.11, 0.81
muf1_Fake_1L_0J_RISR	+0.11, 0.98
muf1_Fake_1L_0J_Mperp	-0.27, 0.99

Table A.2: Pulls for light flavor/unmatched fake muon shape nuisance parameters for fit to 2016 data.

b-only fit	
name	$\Delta x/\sigma_{\text{in}}$, $\sigma_{\text{out}}/\sigma_{\text{in}}$
elf1_Fake_3L_inclJS_RISR	-0.01, 1.00
elf1_Fake_3L_0J_RISR	+0.08, 0.99
elf1_Fake_2L_2J_RISR	+0.30, 0.64
elf1_Fake_2L_2J_Mperp	+0.01, 0.63
elf1_Fake_2L_1J_RISR	+0.65, 0.62
elf1_Fake_2L_1J_Mperp	-0.42, 0.68
elf1_Fake_2L_0J_RISR	+1.23, 0.69
elf1_Fake_2L_0J_Mperp	+1.50, 0.74
elf1_Fake_1L_ge4J_RISR	+0.00, 0.89
elf1_Fake_1L_ge4J_Mperp	-0.41, 0.91
elf1_Fake_1L_3J_RISR	-0.33, 0.85
elf1_Fake_1L_3J_Mperp	-0.96, 0.87
elf1_Fake_1L_2J_RISR	-0.69, 0.77
elf1_Fake_1L_2J_Mperp	-0.89, 0.82
elf1_Fake_1L_1J_RISR	+0.60, 0.79
elf1_Fake_1L_1J_Mperp	+0.22, 0.80
elf1_Fake_1L_0J_RISR	+0.18, 0.90
elf1_Fake_1L_0J_Mperp	+0.28, 0.94

Table A.3: Pulls for light flavor/unmatched fake electron shape nuisance parameters for fit to 2016 data.

b-only fit	
name	$\Delta x/\sigma_{\text{in}}$, $\sigma_{\text{out}}/\sigma_{\text{in}}$
elf0_Fake_3L_inclJS_RISR	-0.02, 1.00
elf0_Fake_3L_0J_RISR	+0.14, 0.99
elf0_Fake_2L_2J_RISR	+0.39, 0.92
elf0_Fake_2L_2J_Mperp	-0.14, 0.92
elf0_Fake_2L_1J_RISR	+0.24, 0.93
elf0_Fake_2L_1J_Mperp	-0.02, 0.96
elf0_Fake_2L_0J_RISR	+0.64, 0.96
elf0_Fake_2L_0J_Mperp	+0.68, 0.95
elf0_Fake_1L_ge4J_RISR	+0.00, 0.99
elf0_Fake_1L_ge4J_Mperp	-0.10, 0.99
elf0_Fake_1L_3J_RISR	+0.02, 0.99
elf0_Fake_1L_3J_Mperp	-0.31, 1.00
elf0_Fake_1L_2J_RISR	-0.13, 0.99
elf0_Fake_1L_2J_Mperp	-0.15, 0.99
elf0_Fake_1L_1J_RISR	+0.11, 1.00
elf0_Fake_1L_1J_Mperp	+0.05, 1.00
elf0_Fake_1L_0J_RISR	-0.02, 1.00
elf0_Fake_1L_0J_Mperp	+0.02, 1.00

Table A.4: Pulls for heavy flavor fake electron shape nuisance parameters for fit to 2016 data.

b-only fit	
name	$\Delta x/\sigma_{\text{in}}$, $\sigma_{\text{out}}/\sigma_{\text{in}}$
norm_bkgs_3L_1jS	+0.25, 0.33
norm_bkgs_3L_0jS	+0.85, 0.31
norm_bkgs_2L_2jS	-0.02, 0.09
norm_bkgs_2L_1jS	+0.28, 0.26
norm_bkgs_2L_0jS	+0.26, 0.13
norm_bkgs_1L_4jS	-0.03, 0.12
norm_bkgs_1L_3jS	-0.03, 0.09
norm_bkgs_1L_2jS	-0.04, 0.07
norm_bkgs_1L_1jS	+0.77, 0.25
norm_bkgs_1L_0jS	+0.08, 0.07
norm_bkgs_0L_5jS	+0.10, 0.23
norm_bkgs_0L_4jS	+0.52, 0.16
norm_bkgs_0L_3jS	+0.37, 0.14
norm_bkgs_0L_2jS	+0.32, 0.10
norm_bkgs_0L_1jS	+0.63, 0.24
norm_bkgs_0L_0jS	-0.14, 0.57

Table A.5: Pulls for by process normalization nuisance parameters for fit to 2016 data.

b-only fit	
name	$\Delta x/\sigma_{\text{in}}$, $\sigma_{\text{out}}/\sigma_{\text{in}}$
norm_QCD_2L_2jS	-0.01, 0.98
norm_QCD_2L_1jS	-1.43, 0.78
norm_QCD_2L_0jS	+0.06, 1.00
norm_QCD_1L_4jS	+0.28, 0.62
norm_QCD_1L_3jS	-0.25, 0.52
norm_QCD_1L_2jS	+0.34, 0.48
norm_QCD_1L_1jS	+0.29, 0.66
norm_QCD_0L_5jS	-0.03, 0.64
norm_QCD_0L_4jS	-0.18, 0.60
norm_QCD_0L_3jS	-0.02, 0.53
norm_QCD_0L_2jS	+0.30, 0.54
norm_QCD_0L_1jS	+1.14, 0.48
QCD_5J_RISR	-0.88, 0.75
QCD_5J_Mperp	-0.91, 0.94
QCD_4J_RISR	-0.03, 0.68
QCD_4J_Mperp	-1.39, 0.53
QCD_3J_RISR	-0.33, 0.31
QCD_3J_Mperp	-0.99, 0.41
QCD_2J_RISR	+0.85, 0.36
QCD_2J_Mperp	-1.62, 0.61
QCD_1J_RISR	-0.38, 0.76
QCD_1J_Mperp	-0.20, 0.79

Table A.6: Pulls for QCD normalization and shape nuisance parameters for fit to 2016 data.

b-only fit	
name	$\Delta x/\sigma_{\text{in}}$, $\sigma_{\text{out}}/\sigma_{\text{in}}$
sig_xsec	+0.00, 1.00
scale_TB	+0.34, 1.03
scale_ST	+1.59, 0.52
lumi_2016	+0.23, 0.99
gamT_2L_23jS	-0.24, 0.52
gamT_2L_01jS	+1.20, 0.40
gamT_1L_234jS	-0.23, 0.23
gamT_1L_01jS	-0.21, 0.20
gamT_0L_2345jS	-0.38, 0.75
gamT_0L_01jS	-0.38, 0.75
SV_eta_top	+0.22, 0.97
SV_eta_other	-0.16, 0.86
SV_eff	-1.20, 0.37
PTISR_1L_4jS	+0.22, 0.33
PTISR_1L_3jS	+0.22, 0.29
PTISR_1L_2jS	+0.04, 0.23
PTISR_1L_1jS	-1.97, 0.16
PTISR_1L_0jS	-0.31, 0.28
PTISR_0L_5jS	+0.79, 0.44
PTISR_0L_4jS	-0.24, 0.36
PTISR_0L_3jS	+0.44, 0.27
PTISR_0L_2jS	+0.03, 0.26
PTISR_0L_1jS	-1.59, 0.21
Fakes_muf1	+1.14, 0.12
Fakes_muf0	+0.53, 0.26
Fakes_elf1	+0.80, 0.15
Fakes_elf0	-0.62, 0.45

Table A.7: Pulls for other normalization nuisance parameters for fit to 2016 data.

A.2 2017 Pulls

b-only fit	
name	$\Delta x/\sigma_{\text{in}}$, $\sigma_{\text{out}}/\sigma_{\text{in}}$
muf0_Fake_3L_inclJS_RISR	+0.05, 1.00
muf0_Fake_3L_0J_RISR	+0.46, 0.95
muf0_Fake_2L_2J_RISR	+0.70, 0.70
muf0_Fake_2L_2J_Mperp	+0.73, 0.69
muf0_Fake_2L_1J_RISR	+0.05, 0.74
muf0_Fake_2L_1J_Mperp	+0.86, 0.79
muf0_Fake_2L_0J_RISR	+1.27, 0.83
muf0_Fake_2L_0J_Mperp	+0.17, 0.89
muf0_Fake_1L_ge4J_RISR	-1.09, 0.97
muf0_Fake_1L_ge4J_Mperp	-0.99, 0.98
muf0_Fake_1L_3J_RISR	-0.17, 0.95
muf0_Fake_1L_3J_Mperp	+0.12, 0.95
muf0_Fake_1L_2J_RISR	-0.08, 0.97
muf0_Fake_1L_2J_Mperp	+0.28, 0.96
muf0_Fake_1L_1J_RISR	-0.07, 0.98
muf0_Fake_1L_1J_Mperp	-0.11, 0.97
muf0_Fake_1L_0J_RISR	-0.34, 0.99
muf0_Fake_1L_0J_Mperp	+0.32, 0.99

Table A.8: Pulls for heavy flavor fake muon shape nuisance parameters for fit to 2017 data.

b-only fit	
name	$\Delta x/\sigma_{\text{in}}$, $\sigma_{\text{out}}/\sigma_{\text{in}}$
muf1_Fake_3L_inclJS_RISR	+0.32, 0.96
muf1_Fake_3L_0J_RISR	+0.46, 0.96
muf1_Fake_2L_2J_RISR	+1.47, 0.60
muf1_Fake_2L_2J_Mperp	-0.08, 0.60
muf1_Fake_2L_1J_RISR	+0.42, 0.60
muf1_Fake_2L_1J_Mperp	+1.03, 0.69
muf1_Fake_2L_0J_RISR	-0.05, 0.62
muf1_Fake_2L_0J_Mperp	+0.57, 0.82
muf1_Fake_1L_ge4J_RISR	-2.49, 0.75
muf1_Fake_1L_ge4J_Mperp	-1.62, 0.80
muf1_Fake_1L_3J_RISR	-0.79, 0.81
muf1_Fake_1L_3J_Mperp	+0.30, 0.79
muf1_Fake_1L_2J_RISR	-0.32, 0.84
muf1_Fake_1L_2J_Mperp	+0.56, 0.82
muf1_Fake_1L_1J_RISR	-0.53, 0.84
muf1_Fake_1L_1J_Mperp	-0.49, 0.86
muf1_Fake_1L_0J_RISR	-0.50, 0.98
muf1_Fake_1L_0J_Mperp	+0.47, 0.98

Table A.9: Pulls for light flavor/unmatched fake muon shape nuisance parameters for fit to 2017 data.

b-only fit	
name	$\Delta x/\sigma_{\text{in}}$, $\sigma_{\text{out}}/\sigma_{\text{in}}$
elf1_Fake_3L_inclJS_RISR	+0.04, 1.00
elf1_Fake_3L_0J_RISR	+0.04, 1.00
elf1_Fake_2L_2J_RISR	+0.67, 0.77
elf1_Fake_2L_2J_Mperp	+0.28, 0.79
elf1_Fake_2L_1J_RISR	+0.75, 0.79
elf1_Fake_2L_1J_Mperp	+0.97, 0.81
elf1_Fake_2L_0J_RISR	+0.89, 0.83
elf1_Fake_2L_0J_Mperp	+1.51, 0.82
elf1_Fake_1L_ge4J_RISR	+0.19, 0.95
elf1_Fake_1L_ge4J_Mperp	-0.13, 0.95
elf1_Fake_1L_3J_RISR	-0.10, 0.91
elf1_Fake_1L_3J_Mperp	+0.20, 0.92
elf1_Fake_1L_2J_RISR	-0.58, 0.87
elf1_Fake_1L_2J_Mperp	-0.22, 0.89
elf1_Fake_1L_1J_RISR	+0.32, 0.88
elf1_Fake_1L_1J_Mperp	+0.86, 0.86
elf1_Fake_1L_0J_RISR	-0.49, 0.97
elf1_Fake_1L_0J_Mperp	+0.37, 0.99

Table A.10: Pulls for light flavor/unmatched fake electron shape nuisance parameters for fit to 2017 data.

b-only fit	
name	$\Delta x/\sigma_{\text{in}}$, $\sigma_{\text{out}}/\sigma_{\text{in}}$
elf0_Fake_3L_inclJS_RISR	+0.04, 1.00
elf0_Fake_3L_0J_RISR	+0.10, 0.99
elf0_Fake_2L_2J_RISR	+0.91, 0.85
elf0_Fake_2L_2J_Mperp	+0.31, 0.87
elf0_Fake_2L_1J_RISR	+0.67, 0.90
elf0_Fake_2L_1J_Mperp	+0.90, 0.93
elf0_Fake_2L_0J_RISR	+0.60, 0.96
elf0_Fake_2L_0J_Mperp	+0.90, 0.93
elf0_Fake_1L_ge4J_RISR	+0.07, 0.99
elf0_Fake_1L_ge4J_Mperp	+0.01, 0.99
elf0_Fake_1L_3J_RISR	+0.05, 0.98
elf0_Fake_1L_3J_Mperp	+0.06, 0.98
elf0_Fake_1L_2J_RISR	-0.20, 0.99
elf0_Fake_1L_2J_Mperp	-0.15, 0.98
elf0_Fake_1L_1J_RISR	+0.08, 0.99
elf0_Fake_1L_1J_Mperp	+0.15, 1.00
elf0_Fake_1L_0J_RISR	-0.11, 1.00
elf0_Fake_1L_0J_Mperp	+0.08, 1.00

Table A.11: Pulls for heavy flavor fake electron shape nuisance parameters for fit to 2017 data.

b-only fit	
name	$\Delta x/\sigma_{\text{in}}$, $\sigma_{\text{out}}/\sigma_{\text{in}}$
norm_bkgs_3L_1jS	+1.30, 0.54
norm_bkgs_3L_0jS	-0.90, 0.37
norm_bkgs_2L_2jS	+0.46, 0.15
norm_bkgs_2L_1jS	+1.08, 0.51
norm_bkgs_2L_0jS	-0.78, 0.23
norm_bkgs_1L_4jS	+1.43, 0.17
norm_bkgs_1L_3jS	+0.99, 0.14
norm_bkgs_1L_2jS	+0.43, 0.12
norm_bkgs_1L_1jS	+1.07, 0.50
norm_bkgs_1L_0jS	-0.32, 0.45
norm_bkgs_0L_5jS	+1.70, 0.31
norm_bkgs_0L_4jS	+1.17, 0.28
norm_bkgs_0L_3jS	+0.98, 0.25
norm_bkgs_0L_2jS	+0.98, 0.23
norm_bkgs_0L_1jS	+0.67, 0.52
norm_bkgs_0L_0jS	+0.35, 0.65

Table A.12: Pulls for by process normalization nuisance parameters for fit to 2017 data.

b-only fit	
name	$\Delta x/\sigma_{\text{in}}$, $\sigma_{\text{out}}/\sigma_{\text{in}}$
norm_QCD_2L_2jS	+1.14, 0.77
norm_QCD_2L_1jS	-0.01, 0.78
norm_QCD_2L_0jS	-2.03, 0.80
norm_QCD_1L_4jS	-0.51, 0.48
norm_QCD_1L_3jS	-0.35, 0.45
norm_QCD_1L_2jS	-0.42, 0.42
norm_QCD_1L_1jS	-0.33, 0.67
norm_QCD_1L_0jS	-0.25, 0.93
norm_QCD_0L_5jS	-0.07, 0.53
norm_QCD_0L_4jS	+0.41, 0.53
norm_QCD_0L_3jS	+0.18, 0.40
norm_QCD_0L_2jS	+0.01, 0.40
norm_QCD_0L_1jS	+0.34, 0.65
QCD_5J_RISR	-0.50, 0.76
QCD_5J_Mperp	-1.05, 0.50
QCD_4J_RISR	-0.93, 0.78
QCD_4J_Mperp	-0.97, 0.31
QCD_3J_RISR	-1.59, 0.30
QCD_3J_Mperp	-0.41, 0.25
QCD_2J_RISR	-1.13, 0.33
QCD_2J_Mperp	-1.18, 0.32
QCD_1J_RISR	-1.24, 0.55
QCD_1J_Mperp	-0.38, 0.80
QCD_0J_RISR	-0.22, 0.98
QCD_0J_Mperp	+0.19, 1.01

Table A.13: Pulls for QCD normalization and shape nuisance parameters for fit to 2017 data.

b-only fit	
name	$\Delta x/\sigma_{\text{in}}$, $\sigma_{\text{out}}/\sigma_{\text{in}}$
norm_Wjets_3L_1jS	+1.09, 0.95
norm_Wjets_3L_0jS	-0.20, 0.94
norm_Wjets_2L_2jS	+0.91, 0.54
norm_Wjets_2L_1jS	-1.08, 0.66
norm_Wjets_2L_0jS	+0.47, 0.44
norm_Wjets_1L_4jS	+3.01, 0.21
norm_Wjets_1L_3jS	+1.42, 0.14
norm_Wjets_1L_2jS	+0.69, 0.09
norm_Wjets_1L_1jS	+0.14, 0.60
norm_Wjets_1L_0jS	+0.37, 0.09
norm_Wjets_0L_5jS	+6.49, 0.38
norm_Wjets_0L_4jS	+3.52, 0.35
norm_Wjets_0L_3jS	+2.64, 0.32
norm_Wjets_0L_2jS	+0.12, 0.32
norm_Wjets_0L_1jS	-0.15, 0.63
norm_Wjets_0L_0jS	+0.25, 0.94

Table A.14: Pulls for W + jets normalization nuisance parameters for fit to 2017 data.

b-only fit	
name	$\Delta x/\sigma_{\text{in}}$, $\sigma_{\text{out}}/\sigma_{\text{in}}$
sig_xsec	-0.00, 1.00
scale_TB	+1.89, 1.24
scale_ST	+2.23, 0.56
lumi_2017	+0.49, 1.00
gamT_2L_23jS	+0.05, 0.54
gamT_2L_01jS	+0.16, 0.42
gamT_1L_234jS	+0.50, 0.22
gamT_1L_01jS	-0.67, 0.19
gamT_0L_2345jS	+0.05, 0.71
gamT_0L_01jS	+0.05, 0.71
SV_eta_top	-0.42, 0.94
SV_eta_other	-2.82, 0.72
SV_eff	-1.77, 0.28
PTISR_1L_4jS	+0.02, 0.30
PTISR_1L_3jS	+0.03, 0.26
PTISR_1L_2jS	+0.33, 0.21
PTISR_1L_1jS	-0.25, 0.15
PTISR_1L_0jS	-0.08, 0.27
PTISR_0L_5jS	+0.53, 0.39
PTISR_0L_4jS	+0.20, 0.33
PTISR_0L_3jS	-0.14, 0.27
PTISR_0L_2jS	-0.16, 0.26
PTISR_0L_1jS	-0.54, 0.21
Fakes_muf1	+1.20, 0.15
Fakes_muf0	+2.22, 0.23
Fakes_elf1	+0.28, 0.25
Fakes_elf0	-0.28, 0.44

Table A.15: Pulls for other normalization nuisance parameters for fit to 2017 data.

A.3 2018 Pulls

b-only fit	
name	$\Delta x/\sigma_{\text{in}}$, $\sigma_{\text{out}}/\sigma_{\text{in}}$
muf0_Fake_3L_inclJS_RISR	-0.04, 0.99
muf0_Fake_3L_0J_RISR	-0.11, 0.90
muf0_Fake_2L_2J_RISR	-0.23, 0.49
muf0_Fake_2L_2J_Mperp	+0.10, 0.48
muf0_Fake_2L_1J_RISR	+0.61, 0.55
muf0_Fake_2L_1J_Mperp	-0.38, 0.66
muf0_Fake_2L_0J_RISR	+0.08, 0.65
muf0_Fake_2L_0J_Mperp	-1.30, 0.75
muf0_Fake_1L_ge4J_RISR	-2.37, 0.85
muf0_Fake_1L_ge4J_Mperp	-1.90, 0.90
muf0_Fake_1L_3J_RISR	+0.68, 0.87
muf0_Fake_1L_3J_Mperp	-0.40, 0.89
muf0_Fake_1L_2J_RISR	+1.27, 0.90
muf0_Fake_1L_2J_Mperp	+0.68, 0.87
muf0_Fake_1L_1J_RISR	+1.15, 0.94
muf0_Fake_1L_1J_Mperp	+0.42, 0.93
muf0_Fake_1L_0J_RISR	+1.14, 0.96
muf0_Fake_1L_0J_Mperp	-2.41, 0.98

Table A.16: Pulls for heavy flavor fake muon shape nuisance parameters for fit to 2018 data.

b-only fit	
name	$\Delta x/\sigma_{\text{in}}$, $\sigma_{\text{out}}/\sigma_{\text{in}}$
muf1_Fake_3L_inclJS_RISR	+0.08, 0.96
muf1_Fake_3L_0J_RISR	+0.02, 0.97
muf1_Fake_2L_2J_RISR	+1.51, 0.79
muf1_Fake_2L_2J_Mperp	-1.31, 0.80
muf1_Fake_2L_1J_RISR	-0.43, 0.75
muf1_Fake_2L_1J_Mperp	-3.29, 0.83
muf1_Fake_2L_0J_RISR	+0.13, 0.79
muf1_Fake_2L_0J_Mperp	-3.87, 0.88
muf1_Fake_1L_ge4J_RISR	-2.54, 0.82
muf1_Fake_1L_ge4J_Mperp	-1.60, 0.87
muf1_Fake_1L_3J_RISR	+0.82, 0.82
muf1_Fake_1L_3J_Mperp	-0.12, 0.81
muf1_Fake_1L_2J_RISR	+1.65, 0.79
muf1_Fake_1L_2J_Mperp	+0.77, 0.75
muf1_Fake_1L_1J_RISR	+1.77, 0.83
muf1_Fake_1L_1J_Mperp	+0.04, 0.89
muf1_Fake_1L_0J_RISR	+0.81, 0.98
muf1_Fake_1L_0J_Mperp	-1.28, 1.00

Table A.17: Pulls for light flavor/unmatched fake muon shape nuisance parameters for fit to 2018 data.

b-only fit	
name	$\Delta x/\sigma_{\text{in}}$, $\sigma_{\text{out}}/\sigma_{\text{in}}$
elf1_Fake_3L_inclJS_RISR	-0.01, 0.99
elf1_Fake_3L_0J_RISR	-0.04, 0.97
elf1_Fake_2L_2J_RISR	+4.40, 0.43
elf1_Fake_2L_2J_Mperp	-0.91, 0.37
elf1_Fake_2L_1J_RISR	+1.19, 0.41
elf1_Fake_2L_1J_Mperp	+3.30, 0.48
elf1_Fake_2L_0J_RISR	-0.88, 0.46
elf1_Fake_2L_0J_Mperp	+1.12, 0.57
elf1_Fake_1L_ge4J_RISR	-1.94, 0.57
elf1_Fake_1L_ge4J_Mperp	-0.18, 0.60
elf1_Fake_1L_3J_RISR	-2.14, 0.51
elf1_Fake_1L_3J_Mperp	-0.54, 0.53
elf1_Fake_1L_2J_RISR	-3.49, 0.37
elf1_Fake_1L_2J_Mperp	-2.94, 0.38
elf1_Fake_1L_1J_RISR	-4.58, 0.34
elf1_Fake_1L_1J_Mperp	-5.56, 0.33
elf1_Fake_1L_0J_RISR	-1.57, 0.61
elf1_Fake_1L_0J_Mperp	+5.92, 0.80

Table A.18: Pulls for light flavor/unmatched fake electron shape nuisance parameters for fit to 2018 data.

b-only fit	
name	$\Delta x/\sigma_{\text{in}}$, $\sigma_{\text{out}}/\sigma_{\text{in}}$
elf0_Fake_3L_inclJS_RISR	-0.00, 1.00
elf0_Fake_3L_0J_RISR	-0.00, 1.00
elf0_Fake_2L_2J_RISR	-0.13, 0.99
elf0_Fake_2L_2J_Mperp	+0.01, 1.00
elf0_Fake_2L_1J_RISR	+0.09, 1.00
elf0_Fake_2L_1J_Mperp	+0.23, 1.00
elf0_Fake_2L_0J_RISR	-0.01, 1.00
elf0_Fake_2L_0J_Mperp	+0.20, 1.00
elf0_Fake_1L_ge4J_RISR	-0.05, 1.00
elf0_Fake_1L_ge4J_Mperp	-0.02, 1.00
elf0_Fake_1L_3J_RISR	-0.06, 1.00
elf0_Fake_1L_3J_Mperp	+0.02, 1.00
elf0_Fake_1L_2J_RISR	-0.03, 1.00
elf0_Fake_1L_2J_Mperp	-0.12, 1.00
elf0_Fake_1L_1J_RISR	-0.05, 1.00
elf0_Fake_1L_1J_Mperp	-0.07, 1.00
elf0_Fake_1L_0J_RISR	-0.04, 1.00
elf0_Fake_1L_0J_Mperp	+0.05, 1.00

Table A.19: Pulls for heavy flavor fake electron shape nuisance parameters for fit to 2018 data.

b-only fit	
name	$\Delta x/\sigma_{\text{in}}$, $\sigma_{\text{out}}/\sigma_{\text{in}}$
norm_bkgs_3L_1jS	-1.27, 0.49
norm_bkgs_3L_0jS	-0.19, 0.30
norm_bkgs_2L_2jS	+0.22, 0.10
norm_bkgs_2L_1jS	+0.41, 0.47
norm_bkgs_2L_0jS	-0.39, 0.19
norm_bkgs_1L_4jS	+1.06, 0.14
norm_bkgs_1L_3jS	+0.39, 0.12
norm_bkgs_1L_2jS	+0.14, 0.10
norm_bkgs_1L_1jS	+2.18, 0.47
norm_bkgs_1L_0jS	-0.56, 0.31
norm_bkgs_0L_5jS	+1.15, 0.25
norm_bkgs_0L_4jS	-1.00, 0.25
norm_bkgs_0L_3jS	-0.88, 0.20
norm_bkgs_0L_2jS	-0.62, 0.16
norm_bkgs_0L_1jS	+2.97, 0.49
norm_bkgs_0L_0jS	-0.18, 0.39

Table A.20: Pulls for by process normalization nuisance parameters for fit to 2018 data.

b-only fit	
name	$\Delta x/\sigma_{\text{in}}$, $\sigma_{\text{out}}/\sigma_{\text{in}}$
norm_QCD_3L_1jS	-1.05, 0.82
norm_QCD_2L_2jS	+2.29, 0.63
norm_QCD_2L_1jS	-1.99, 0.64
norm_QCD_2L_0jS	+0.35, 1.07
norm_QCD_1L_4jS	-1.08, 0.39
norm_QCD_1L_3jS	-0.92, 0.38
norm_QCD_1L_2jS	-0.74, 0.37
norm_QCD_1L_1jS	+0.35, 0.60
norm_QCD_1L_0jS	+0.45, 0.63
norm_QCD_0L_5jS	-2.25, 0.41
norm_QCD_0L_4jS	-4.30, 0.21
norm_QCD_0L_3jS	-1.96, 0.20
norm_QCD_0L_2jS	-1.13, 0.18
norm_QCD_0L_1jS	+2.68, 0.58
QCD_5J_RISR	-1.85, 0.75
QCD_5J_Mperp	-2.28, 0.23
QCD_4J_RISR	-1.90, 0.19
QCD_4J_Mperp	-1.64, 0.19
QCD_3J_RISR	-1.26, 0.16
QCD_3J_Mperp	-0.24, 0.16
QCD_2J_RISR	-0.26, 0.13
QCD_2J_Mperp	-0.32, 0.15
QCD_1J_RISR	-0.16, 0.28
QCD_1J_Mperp	+0.20, 0.66
QCD_0J_RISR	-0.28, 0.89
QCD_0J_Mperp	+0.05, 0.99

Table A.21: Pulls for QCD normalization and shape nuisance parameters for fit to 2018 data.

b-only fit	
name	$\Delta x/\sigma_{\text{in}}$, $\sigma_{\text{out}}/\sigma_{\text{in}}$
norm_Wjets_3L_1jS	+0.86, 1.00
norm_Wjets_3L_0jS	+0.18, 1.00
norm_Wjets_2L_2jS	-3.63, 0.79
norm_Wjets_2L_1jS	-4.41, 0.69
norm_Wjets_2L_0jS	+5.33, 0.55
norm_Wjets_1L_4jS	+2.48, 0.21
norm_Wjets_1L_3jS	+0.82, 0.15
norm_Wjets_1L_2jS	+0.53, 0.09
norm_Wjets_1L_1jS	+5.74, 0.61
norm_Wjets_1L_0jS	+0.46, 0.08
norm_Wjets_0L_5jS	+15.68, 0.37
norm_Wjets_0L_4jS	+15.67, 0.29
norm_Wjets_0L_3jS	+13.56, 0.30
norm_Wjets_0L_2jS	+9.37, 0.33
norm_Wjets_0L_1jS	-2.20, 0.63
norm_Wjets_0L_0jS	+0.11, 1.01

Table A.22: Pulls for W + jets normalization nuisance parameters for fit to 2018 data.

b-only fit	
name	$\Delta x/\sigma_{\text{in}}$, $\sigma_{\text{out}}/\sigma_{\text{in}}$
sig_xsec	+0.00, 1.00
scale_TB	+1.44, 1.15
scale_ST	+2.85, 0.52
lumi_2018	+0.51, 1.00
gamT_2L_23jS	+0.99, 0.49
gamT_2L_01jS	+0.76, 0.38
gamT_1L_234jS	-0.34, 0.19
gamT_1L_01jS	-1.02, 0.17
gamT_0L_2345jS	-0.50, 0.71
gamT_0L_01jS	-0.50, 0.71
SV_eta_top	+0.09, 0.93
SV_eta_other	-2.68, 0.70
SV_eff	-0.15, 0.23
PTISR_1L_4jS	-0.53, 0.24
PTISR_1L_3jS	+0.32, 0.22
PTISR_1L_2jS	+0.14, 0.17
PTISR_1L_1jS	-2.13, 0.12
PTISR_1L_0jS	+0.55, 0.24
PTISR_0L_5jS	-1.72, 0.31
PTISR_0L_4jS	-0.18, 0.26
PTISR_0L_3jS	-0.64, 0.21
PTISR_0L_2jS	-0.59, 0.20
PTISR_0L_1jS	-0.87, 0.18
Fakes_muf1	+1.17, 0.12
Fakes_muf0	+4.38, 0.13
Fakes_elf1	+6.43, 0.06
Fakes_elf0	-5.06, 0.62

Table A.23: Pulls for other normalization nuisance parameters for fit to 2018 data.